International Journal of Nanomedicine

Dovepress
Taylor & Francis Group

Open Access Full Text Article

ORIGINAL RESEARCH

Blackberry-Like Doxorubicin Loaded Hyaluronic Acid/Zinc Phthalocyanine Loaded Mesoporous Silica Nanocomposites for Long-Term Tumor Photodynamic and Chemotherapy Synergistic Therapy

Shangting Du[1], Lingyu Li[1], Junhao Kou[2], Tianyi Zhu[1], Zhenyi Song[2], Yonghua Zhan[3], Daocheng Wu[4], Wenhua Zhan[1,5]

[1]Department of Radiation Oncology, General Hospital of Ningxia Medical University, Yinchuan, Ningxia Hui Autonomous Region, 750004, People's Republic of China; [2]School of Pharmacy, Xi'an Medical University, Xi'an, Shaanxi, 710021, People's Republic of China; [3]School of Life Science and Technology, Xidian University and Engineering Research Center of Molecular and Neuro Imaging, Ministry of Education, Xi'an, Shaanxi, 710071, People's Republic of China; [4]Key Laboratory of Biomedical Information Engineering of the Ministry of Education, School of Life Science and Technology, Xi'an Jiaotong University, Xi'an, Shaanxi, 710049, People's Republic of China; [5]State Key Laboratory of Pathogenesis, Prevention and Treatment of High Incidence Diseases in Central Asia, Xinjiang Medical University, Urumqi, Xinjiang Uygur Autonomous Region, 830054, People's Republic of China

Correspondence: Daocheng Wu, Key Laboratory of Biomedical Information Engineering of the Ministry of Education, School of Life Science and Technology, Xi'an Jiaotong University, Xi'an, Shaanxi, 710049, People's Republic of China, Email wudaocheng@mail.xjtu.edu.cn; Wenhua Zhan, Department of Radiation Oncology, General Hospital of Ningxia Medical University, Yinchuan, Ningxia Hui Autonomous Region, 750004, People's Republic of China, Email zhanwhgood@163.com

Background: The co-loading of zinc phthalocyanine (ZnPc) and doxorubicin (DOX) on a nanocarrier for tumor photodynamic therapy (PDT)-chemotherapy (CT) synergistic therapy is an effective approach. However, significant differences in water solubility between DOX and ZnPc hinder their high drug-loading content within a unified carrier. Additionally, DOX's systemic toxicity limits its therapeutic dosage, while low ZnPc loading shortens PDT duration, collectively restricting the efficacy of PDT and related synergistic therapy. This study aims to design a long-term PDT and CT synergistic therapy strategy to significantly improve the therapeutic effect and reduce the toxic side effects.

Methods: We encapsulated ZnPc within biodegradable mesoporous silica nanoparticles (bMSN NPs) as the core, followed by electrostatic coating with tumor-targeting, DOX-loaded hyaluronic acid nanoparticles (DOX-HA NPs) to fabricate blackberry-like nanocomposites (DOX-HA/ZnPc-bMSN). In vitro and in vivo experiments determined tumor long-term PDT and CT synergistic therapy efficacy with DOX-HA/ZnPc-bMSN.

Results: These nanocomposites achieved high ZnPc loading (DLC: 10.2% ± 1.6%) and efficient tumor accumulation, enabling prolonged systemic circulation (> 96 h) and sustained dual-drug release in vivo, realizing long-term photodynamic and CT synergistic therapy. In vitro studies showed a low combination index (CI = 0.26), with reactive oxygen species (ROS) production enhanced by 1.6-fold and 1.9-fold for ZnPc and DOX. The median lethal dose (LD50) of DOX-HA/ZnPc-bMSN nanocomposites (138.95 mg/kg) was 15.12 times higher than that of free DOX. Notably, in vivo studies demonstrated a 96.0% tumor inhibition rate has been achieved using ultralow doses of drugs (DOX: 0.2 mg/kg; ZnPc: 2 mg/kg). This long-term PDT and CT synergistic therapy elevated intracellular ROS levels, which not only induced apoptosis in tumor cells but also activated caspase-1, leading to direct GSDMD cleavage, GSDMD-N release, and pyroptotic tumor cell death.

Conclusion: These nanocomposites dually trigger tumor cell apoptosis/pyroptosis, demonstrating potent therapeutic efficacy and safety for clinical translation.

Keywords: blackberry-like nanocomposites, mesoporous silica nanoparticles, photodynamic therapy, chemotherapy, synergistic therapy

Received: 23 March 2025
Accepted: 8 July 2025
Published: 17 July 2025

Graphical Abstract

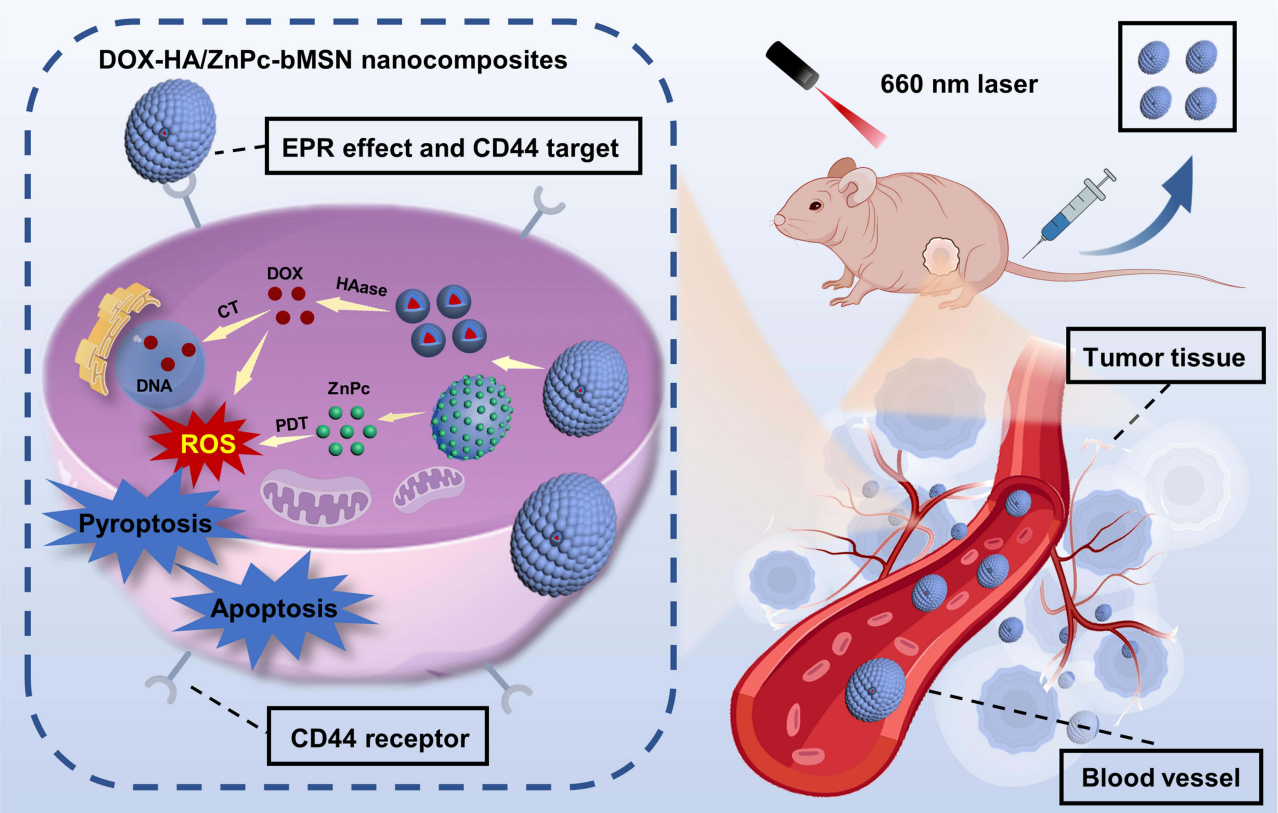

Introduction

Malignant tumors pose a significant threat to human health and survival.[1] Chemotherapy (CT) remains a cornerstone of treatment, characterized by its sustained efficacy (≥ 48 h) and broad-spectrum activity. This therapeutic approach effectively targets tumor cells at both primary and metastatic sites, thereby suppressing tumor progression and dissemination.[2,3] However, the non-specific chemotherapeutic agents lead to several limitations, including suboptimal short-term efficacy, development of drug resistance, and substantial systemic toxicity.[4] Doxorubicin (DOX), a widely utilized broad-spectrum antineoplastic agent, demonstrates therapeutic efficacy against a diverse range of malignancies, including breast carcinoma, prostate tumor, lymphomas, sarcomas, and specific leukemia subtypes.[5] Despite its clinical utility, DOX and related anthracycline compounds are associated with dose-dependent cardiotoxicity, potentially resulting in irreversible myocardial injury.[6] Furthermore, prolonged monotherapy with chemotherapeutic agents may induce drug resistance in neoplastic cells, thereby compromising therapeutic efficacy. Consequently, there exists an imperative clinical need to optimize DOX therapy by minimizing dosage requirements while maximizing therapeutic outcomes. Current strategies for therapeutic enhancement include the utilization of nanocarriers for DOX delivery, which may mitigate adverse effects and prolong therapeutic activity, and the implementation of combination therapies to reduce DOX dosage while achieving synergistic therapeutic effects. Numerous studies have reported the synergistic application of DOX-loaded nanocarriers with other therapies such as hyperthermia, dynamics and immunotherapy.[7–9] Notably, the integration of DOX-loaded nanocarriers with photodynamic therapy (PDT) has emerged as a particularly promising area of investigation, attracting considerable research interest.

PDT represents a useful tumor therapeutic approach, featuring tumor specific targeting, minimal damage to normal tissues, no dark toxicity and repeatability.[10,11] PDT primarily functions through the generation of reactive oxygen species (ROS) by photosensitizers (PS) upon exposure to light of specific wavelengths.[12] However, due to the short half-life of ROS (2–6 hours), the long-term efficacy of PDT alone is suboptimal, necessitating its combination with other therapeutic approaches to enhance treatment outcomes.[13] The synergistic potential of PDT and CT is manifested through their complementary mechanisms: PDT facilitates the rapid generation of substantial ROS within a 2–6 hour window, inducing direct tumor cell cytotoxicity and vascular disruption, while CT provides sustained eradication of residual tumor cells over a 24–48 hour period, thereby mitigating the risks of tumor recurrence and metastatic dissemination. The integration of PDT with CT thus combines the advantages of immediate tumor kill with prolonged tumor suppression, as well as precise local intervention with systemic therapeutic effects, culminating in enhanced therapeutic efficacy and diminished adverse effects.[14,15] Zinc phthalocyanine (ZnPc), a photosensitizer that has progressed to Phase I/II clinical trials in Switzerland for PDT applications, exhibits superior photophysical properties, including pronounced absorption in the near-infrared spectrum (650–800 nm) and exceptional ROS quantum yield. These characteristics render ZnPc particularly suitable for not only superficial tumor treatment, but also for addressing deeper-seated malignancies.[16] However, the clinical utility of ZnPc is constrained by its pronounced hydrophobicity and propensity for crystallization.[17] The co-encapsulation of DOX and ZnPc within a unified nanocarrier system presents a promising approach to achieving PDT-CT synergistic therapy.

Huang et al pioneered a thermosensitive nanoparticle hydrogel (TNPGEL) that successfully co-loaded DOX and ZnPc. The synthesized TNP/DOX/ZnPc demonstrated a marked enhancement in ROS generation and a potent inhibition of tumor cell proliferation, reducing cell viability to a mere 18.5%. Nonetheless, in vivo assessments revealed that while the TNP/DOX/ZnPc cohort exhibited a significantly reduced tumor volume compared to the TNP/DOX and TNP/ZnPc groups, the post-intervention tumor size remained 12.5-fold larger than the pre-treatment volume. This outcome is likely attributable to the suboptimal drug loading content (DLC) of both DOX (0.84%) and ZnPc (0.94%), which may have undermined the therapeutic potential.[18] Wang et al engineered a pH-sensitive nanomicellar platform utilizing folic acid-bile salt-stearic acid (FA-BSP-SA) and tocopheryl polyethylene glycol succinate (TPGS) for the dual loading of DOX and ZnPc. The emulsion-solvent evaporation technique yielded Dox+ZnPc@FA-BSP-SA/TPGS micelles, which boasted a DLC exceeding 6% for DOX but fell short with a ZnPc DLC below 0.5%. This discrepancy was primarily due to the strong hydrophobicity of ZnPc, which caused it to aggregate and precipitate in solution, thereby reducing encapsulation efficiency.[19] Ma et al constructed a drug delivery system based on a ZnPc-soybean phosphatidylcholine (ZnPc-SPC) complex, loaded with DOX (DLC of 9.78%) and modified with methotrexate (MTX) to target folate receptor α (FRα), forming MTX-decorated self-assembled ZnPc-SPC complex NPs (DZSM). In vivo antitumor results indicated that the DZSM group without laser intervention experienced a relative tumor volume exceeding 3.0, whereas the DZSM+laser group saw a modest reduction to just below 1.0.[20] These results imply a less therapeutic contribution from the DOX within DZSM due to DOX's systemic toxicity for normal tissues limiting its therapeutic dosage. Moreover, the limited efficacy observed in the DZSM+laser group may be ascribed to the low loading capacity of ZnPc, which failed to achieve long-term PDT (with a PDT duration of only 15 min) and thus curtailed the full synergistic efficacy between ZnPc and DOX. Therefore, it can be seen that the difference in water solubility between DOX and ZnPc significantly affects the preparation design, and it is difficult to have a carrier material that can meet the high loading capacities of DOX and ZnPc at the same time. The notably low DLC of ZnPc, in particular, precipitates an abbreviated PDT therapeutic window and insufficient chemotherapeutic synergy, significantly detracting from the overall therapeutic efficacy.

In order to overcome the low loading of DOX and ZnPc in the same carrier, we employed biodegradable mesoporous silica nanoparticles (bMSN NPs) for ZnPc encapsulation (bMSN@ZnPc NPs) to obtain bMSN@ZnPc NPs, whereas DOX was loaded into tumor-targeting hyaluronic acid (HA) nanoparticles (DOX-HA NPs). Then DOX-HA NPs were subsequently adsorbed onto the surface of bMSN@ZnPc NPs, resulting in the formation of blackberry-like structured DOX-HA/ZnPc-bMSN nanocomposites (Scheme 1). These bilayer-structured nanocomposites effectively address the limitations arising from the disparate properties of DOX and ZnPc, facilitating high loading of both therapeutic agents within a single system. The modular design allows for precise adjustment of drug concentrations and ratios, making it adaptable to various dual-drug synergistic treatment regimens and therapeutic times. Furthermore, the therapeutic

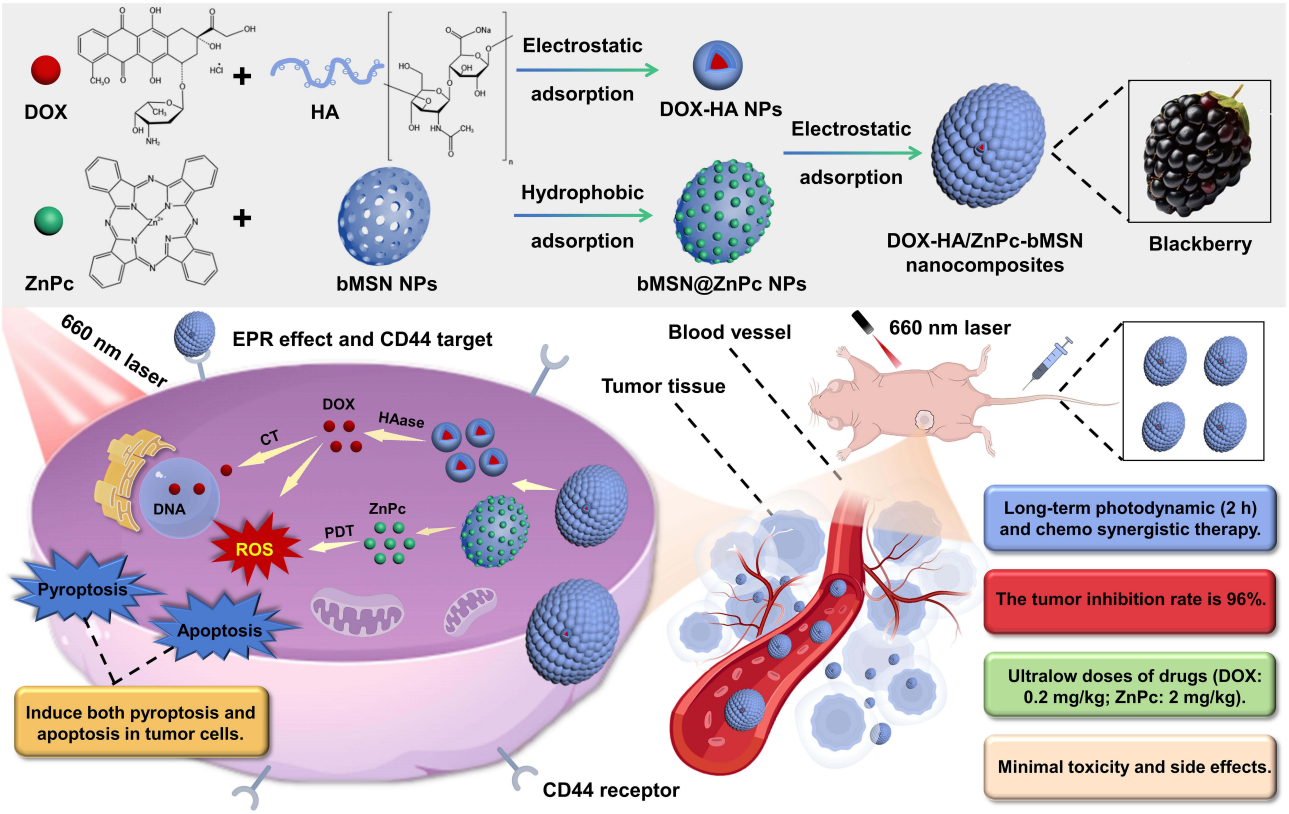

Scheme 1 Preparation of DOX-HA/ZnPc-bMSN nanocomposites and their long-term photodynamic and related chemotherapy synergistic therapy (the blackberry picture designed by tohamina - Freepik.com https://www.freepik.com).

performance can be optimized by systematically refining the structural parameters of the nanocomposites. These nanocomposites not only achieve a high ZnPc loading capacity (DLC of 10.2% ± 1.6%), enabling long-term PDT, but also exhibit exceptional stability and biocompatibility in both in vitro and in vivo.

Benefiting from the tumor-targeting properties of HA and the enhanced permeability and retention (EPR) effects, the nanocomposites demonstrate efficient accumulation at the tumor site, facilitating prolonged systemic circulation (> 96 hours) and sustained release of both DOX and ZnPc in vivo. Following cellular uptake, DOX, positioned on the surface of the nanocomposites, is preferentially released, delivering long-term antitumor activity. Subsequently, ZnPc, encapsulated within the pores of the bMSN NPs, is gradually released, enabling a highly effective and long-lasting PDT effect upon 660 nm laser irradiation. In vitro studies revealed that the nanocomposites exhibit remarkable synergistic efficacy between PDT and related CT, as evidenced by a combination index (CI) of 0.26. The production of ROS in the DOX +ZnPc+laser combination treatment group was enhanced by 1.6-fold and 1.9-fold at the cellular and tissue levels, respectively. In vivo toxicity assessments demonstrated that the nanocomposites possess an exceptionally favorable safety profile, with a median lethal dose (LD50) of 138.95 mg/kg, representing a 15.12-fold increase compared to free DOX (9.19 mg/kg). In vivo antitumor evaluations further highlighted the exceptional therapeutic potential of this approach, achieving a remarkable tumor inhibition rate of 96.0% with ultralow doses of DOX (0.2 mg/kg) and ZnPc (2 mg/kg) combined with prolonged PDT therapy (2 hours). Conventional PDT and CT predominantly exert their antitumor effects by inducing apoptosis in tumor cells.[21,22] Nevertheless, the efficacy of apoptosis induction is frequently constrained by the intrinsic or acquired resistance of tumor cells to apoptotic pathways.[23,24] In contrast to apoptosis, pyroptosis is a form of inflammatory programmed cell death (PCD).[25] Research has demonstrated that inducing pyroptosis in as few as 15% of cells can effectively suppress tumor progression, with ROS recognized as one of the key pathways triggering pyroptosis.[26,27] In this study, the combination of long-term PDT and related synergistic CT via DOX-HA/ZnPc-bMSN nanocomposites significantly augmented the ROS generation capacity of both DOX and ZnPc.

The elevated ROS levels not only promoted apoptosis in PC-3 cells but also triggered pyroptosis through the ROS/caspase-1/GSDMD signaling pathway, substantially enhancing overall PCD efficiency. In summary, the DOX-HA/ZnPc-bMSN nanocomposites along with the long-term PDT and CT synergistic treatment strategy, offer an innovative paradigm for tumor treatment and hold significant potential for clinical development.

Materials and Methods

Materials

Fetal bovine serum (FBS) was purchased from Sigma (Shanghai, China). Trypsin and Dulbecco's modified eagle medium (DMEM) high-glucose culture medium were obtained from Hyclone (Beijing, China). Hexadecyltrimethylammonium chloride (CTAC, 97%), tetraethyl orthosilicate (TEOS), triethylamine (TEA, 99.5%), 3-aminopropyl-trimethoxysilane (APS), DOX (98%), ZnPc, coumarin 6, hyaluronic acid (the average molecular weight: 6.2 kDa), hyaluronidase (HAase), IR-780, and Tween 80 were purchased from Aladdin (Shanghai, China). The Cell Counting Kit-8 (CCK-8), ROS detection kits, lactate dehydrogenase (LDH) cytotoxicity assay kits (WST-8 method), and Calcein/PI cell viability and cytotoxicity assay kits were all purchased from Beyotime Ltd (Shanghai, China). Cleaved caspase-1 antibody (#4199) was obtained from Cell Signaling Technology (CST, Danvers, MA, USA). Cleaved N-terminal GSDMD antibody (ab215203) was acquired from Abcam (Cambridge, MA, USA). The cell lines used included HUVEC, HT-22, and PC-3, which were sourced from Shanghai Coweldgen Scientific Ltd (Shanghai, China) and originated from the American Type Culture Collection (ATCC, Manassas, VA, USA). All experimental animals were obtained from Beijing HFKBio PLC (Beijing, China).

Preparation of bMSN NPs and DOX-HA/ZnPc-bMSN Nanocomposites

The bMSN NPs were prepared via a water-oil two-phase reaction. Briefly, 24 mL of CTAC (25 wt%), 137 μL of TEA, and 34 mL of deionized water were mixed and stirred at 60°C for 1 hour. A mixture of 1 mL TEOS and 19 mL cyclohexane was then added, and the reaction was continued under stirring for 20 hours. The upper cyclohexane layer was carefully removed, and CTAC was eliminated via centrifugation and washing with a NaCl-methanol solution (1 wt %), yielding bMSN NPs. To functionalize the nanoparticles, bMSN NPs were dispersed in 20 mL of anhydrous ethanol, followed by the addition of 1 mL APS. The reaction proceeded at 90°C for 48 hours, after which the precipitate was collected via centrifugation and washed with anhydrous ethanol, forming bMSN-NH_2 NPs. Next, 9 mg of bMSN-NH_2 NPs were dispersed in 5 mL of deionized water, and 1 mg of ZnPc was slowly added under continuous stirring, allowing encapsulation within the nanopores overnight. This process generated positively charged bMSN@ZnPc NPs. For the preparation of DOX-HA NPs, 0.1 mg of DOX was added to 1 mL of HA solution (1 mg/mL in deionized water) and stirred for 10 minutes under neutral conditions, forming negatively charged DOX-HA NPs. Subsequently, the negatively charged DOX-HA NPs were slowly added to the positively charged bMSN@ZnPc NPs under stirring, followed by ultrasonic treatment at 150 W for 10 min with ultrasonic vibrator (Five Phase Instrument & Meter Co Ltd, Shanghai, China). Under the combined action of stirring and ultrasonication, DOX-HA NPs were adsorbed onto the surface of bMSN@ZnPc NPs via electrostatic interaction, resulting in the final blackberry-like nanocomposites: DOX-HA/ZnPc-bMSN nanocomposites.

Due to ZnPc's excellent photochemical properties but poor fluorescence,[28,29] we utilized bMSN NPs loaded with IR-780-a representative hydrophobic near-infrared (NIR) fluorescent dye with a high luminescence quantum yield[30]-to evaluate the in vivo targeting performance of the nanocomposites. The fluorescent nanocomposites were prepared following the same procedure as the DOX-HA/ZnPc-bMSN nanocomposites. Briefly, 9 mg of bMSN-NH_2 NPs were dispersed in 5 mL of deionized water, and 1 mg of IR-780 was slowly added under continuous stirring, allowing adsorption overnight. The negatively charged IR-780 molecules were incorporated into the pores of the positively charged bMSN-NH_2 NPs, forming bMSN@IR780 NPs. These were subsequently combined with DOX-HA NPs via electrostatic interactions, yielding the final negatively charged DOX-HA/IR780-bMSN nanocomposites.

Characteristics of bMSN NPs and DOX-HA/ZnPc-bMSN Nanocomposites

Transmission electron microscopy (TEM, Thermo Fisher Scientific, Waltham, MA, USA) was used to observe the morphology of DOX-HA NPs, bMSN NPs, and DOX-HA/ZnPc-bMSN nanocomposites. The particle size and zeta potential of DOX-HA NPs, bMSN NPs, and DOX-HA/ZnPc-bMSN nanocomposites were measured using a Malvern particle size analyzer (Malvern Instruments Ltd, Worcestershire, UK). The absorption spectra of DOX, ZnPc, and DOX-HA/ZnPc-bMSN nanocomposites were determined using a UV-Vis spectrophotometer (Shanghai Mapada Instruments Co Ltd, Shanghai, China). The chemical structure of DOX, DOX-HA NPs, ZnPc, bMSN NPs, bMSN@ZnPc NPs, and DOX-HA/ZnPc-bMSN nanocomposites was further determined with Fourier transform infrared spectroscopy (FTIR, Bruker Corporation, Billerica, MA, USA). Additionally, the fluorescence spectra of ZnPc and DOX-HA/ZnPc-bMSN nanocomposites at different concentrations were detected using a fluorescence spectrophotometer (B&W TEK Optoelectronics, Shanghai, China). To evaluate the stability of the nanocomposites, bMSN NPs and DOX-HA/ZnPc-bMSN nanocomposites were dispersed in PBS at 4°C, PBS at 37°C, DMEM at 37°C, and FBS at 37°C, and their particle size variations over time were monitored using a Malvern particle size analyzer. High-performance liquid chromatography (HPLC) was used to determine the concentration of the drug, and the encapsulation efficiency (EE) and DLC were calculated according to the following formulas:

$$\mathrm{EE}\ (100\%) = \frac{\mathrm{M_{drug\ input}} - \mathrm{M_{drug\ remain}}}{\mathrm{M_{drug\ input}}} \times 100\%$$

$$\mathrm{DLC}\ (100\%) = \frac{\mathrm{M_{drug\ input}} - \mathrm{M_{drug\ remain}}}{\mathrm{M_{DOX\text{-}HA/ZnPc\text{-}bMSN\ nanocomposites\ input}}} \times 100\%$$

The release profile of DOX from DOX-HA/ZnPc-bMSN nanocomposites was investigated using a dialysis membrane (3500 Da MWCO) in phosphate-buffered saline (PBS, pH = 7.4) under continuous stirring at 100 rpm and 37°C for 72 h. The experimental group consisted of DOX-HA/ZnPc-bMSN nanocomposites, while the control groups included DOX-HA/ZnPc-bMSN nanocomposites treated with 10 U/mL HAase, as well as free DOX, all subjected to the same dialysis conditions. The release profile of ZnPc from the DOX-HA/ZnPc-bMSN nanocomposites was studied under the same experimental conditions and methods, except that the dialysis external solution was supplemented with 1% Tween 80 to enhance its release. Dialysate samples were collected at predetermined time intervals, and the UV-vis absorption was measured at $\lambda = 480$ nm and $\lambda = 660$ nm using a UV-Vis spectrophotometer to determine the release of DOX and ZnPc, respectively. After each sampling, the dialysate was replaced with an equal volume of fresh PBS buffer solution.

Cell Internalization Evaluation of DOX-HA/ZnPc-bMSN Nanocomposites

To effectively observe the internalization of nanocomposites, DOX-HA/ZnPc-bMSN nanocomposites were fluorescently labeled using coumarin 6 (green) and DOX (red). PC-3 cells were seeded into confocal cell dishes and incubated at 37°C in 5% CO_2. After cell adhesion, the fluorescently labeled DOX-HA/ZnPc-bMSN nanocomposites were added and incubated. At 1 h, 2 h, and 4 h, the dishes were treated with 4% paraformaldehyde solution, and the cell nuclei were stained using the DAPI kit. Observations were conducted using a laser confocal microscope (Leica, Wetzlar, Germany). HA could competitively inhibit the internalization of DOX-HA/ZnPc-bMSN nanocomposites. The blocking group of cells was pretreated with HA (5 mg/mL), while the control group received no treatment. Subsequently, DOX-HA/ZnPc-bMSN nanocomposites were added to the confocal cell dishes for incubation. The optimal incubation time was determined based on internalization results. After incubation, the fluorescence was observed with a laser confocal microscope and the fluorescence intensities were measured and quantified using Image J software.

In vitro Toxicity of DOX-HA/ZnPc-bMSN Nanocomposites

Firstly, the cytotoxicity of DOX-HA/ZnPc-bMSN nanocomposites was tested using the CCK-8 assay, including two normal cell lines (HUVEC, HT-22) and the PC-3 cell line. Cells were spread evenly in a 96-well plate at a density of 8000–12,000 cells per well. After adherence, samples were added to each well in a concentration gradient. When the cell density in the control group reached over 80% growth, the medium was replaced with colorless medium containing

CCK-8, and the incubation continued for 1 to 1.5 hours. Absorbance was measured at 450 nm using a microplate reader (Tecan Group Ltd, Männedorf, Switzerland) to calculate cell viability.

The in vitro suppression effect of the DOX-HA/ZnPc-bMSN nanocomposites was evaluated by CCK-8, clone formation, and live/dead cell staining assays. PC-3 cells were seeded into a 24-well plate at 20,000 cells per well. Once the cells reached 50% confluence, different concentrations of DOX-HA/ZnPc-bMSN nanocomposites, ranging from 6.2 μg/mL to 83.3 μg/mL, were added to the dishes, with two experimental groups set at a final concentration of 83.3 μg/mL. Post a 2-hour incubation, each concentration underwent a 2-hour exposure to 660 nm laser light (0.05 W/cm^2), except for one group at 83.3 μg/mL without laser treatment. After an additional 24-hour incubation, cell viability was measured and calculated using the same method.

The proliferation ability of PC-3 cells under different drug treatments was assessed using the colony formation assay. PC-3 cells were seeded into 6 cm culture dishes and incubated overnight at 37°C in 5% CO_2. ZnPc, DOX, ZnPc+DOX, and DOX-HA/ZnPc-bMSN nanocomposites were separately added to the dishes, with concentrations of 40 μg/mL for ZnPc and 4 μg/mL for DOX in each group. The control group remained untreated. After a 2-hour co-incubation of the cells with the drugs, the ZnPc, ZnPc+DOX, and DOX-HA/ZnPc-bMSN nanocomposites' groups were exposed to 660 nm laser light (0.05 W/cm^2) for 2 hours. Fresh culture medium was then replaced after a 12-hour incubation. When the control group displayed at least 50 cloned cells, the cells were fixed and stained, and the number of cloned cells was quantified using Image J software. In the live/dead cell staining test, 60,000 cells were seeded into each well of a 6-well plate. Once the cells reached 90% confluence, they were subjected to various treatments and incubated for an additional 12 hours. Following this, the live/dead cell staining kit was utilized for staining, and the results were observed using an inverted fluorescence microscope. The half-maximal inhibitory concentration (IC50) of ZnPc, DOX, and DOX-HA/ZnPc-bMSN nanocomposites was then calculated using dose-response curves, and the CI of DOX-HA/ZnPc-bMSN nanocomposites was determined using the Chou-Talalay method (Supplementary Material 1).[31]

Inhibiting Efficacy of DOX-HA/ZnPc-bMSN Nanocomposites on the Proliferation of PC-3 Cells

The photodynamic effect of DOX-HA/ZnPc-bMSN nanocomposites in vitro was evaluated through ROS production experiments. PC-3 cells were seeded in a 6-well plate at a density of 40,000 cells per well. After the cells grew to 80% confluence, they were grouped and treated with the corresponding samples and interventions. After a 6-hour incubation, the cells were stained with the ROS probe DCFH-DA, and the fluorescence signals were observed and captured using an inverted fluorescence microscope. Subsequently, flow cytometry was employed to detect apoptosis in PC-3 cells under different treatments. The cultured PC-3 cells were digested, centrifuged, and resuspended, then seeded in a 24-well plate. DOX, ZnPc, DOX+ZnPc, and DOX-HA/ZnPc-bMSN nanocomposites were added, with ZnPc and DOX concentrations set at 20 μg/mL and 2 μg/mL, respectively, and co-incubated for 48 hours. The cells in the treatment groups with ZnPc, DOX+ZnPc, and DOX-HA/ZnPc-bMSN nanocomposites were irradiated with a 660 nm laser (0.05 W/cm^2) for 1 hour, then collected and washed three times with PBS. The cells were then stained with Annexin-V FITC for 1 hour, followed by PI staining for 30 minutes, and finally analyzed using flow cytometer (BD Biosciences, San Jose, CA, USA).

To validate the induction of pyroptosis in PC-3 cells by DOX-HA/ZnPc-bMSN nanocomposites, the morphological changes of PC-3 cells following various treatments were first observed and photographed using an optical microscope (Olympus, Tokyo, Japan). A suitable quantity of PC-3 cells was seeded into a 24-well plate and incubated for 48 hours until reaching approximately 90% confluence. Following this, the cells were subjected to different interventions. After 12 hours, they were observed and photographed under an optical microscope. The expression of pyroptosis-related proteins, including cleaved caspase-1 and cleaved N-terminal GSDMD, was detected in each group of PC-3 cells using Western blotting. After various treatments, proteins from each group of PC-3 cells were extracted. Protein quantification was performed using the Bicinchoninic Acid (BCA) assay, with a loading amount of 30 μg per well. The samples were electrophoresed until the bromophenol blue reached the bottom of the gel, then subjected to wet transfer for membrane transfer, followed by blocking with 5% fat-free milk. The antibodies, including cleaved caspase-1 (CST, #4199) and cleaved N-terminal GSDMD (Abcam, ab215203), were incubated overnight at 4°C. The protein bands were observed

using a protein detection system (Bio-Rad, Hercules, CA, USA). The exposure results were analyzed using Image J software, and all experiments were repeated three times. Further detection of pyroptosis-related inflammatory markers LDH, IL-1β, and IL-18 was performed. The LDH cytotoxicity detection kit (WST-8 method) was used to measure the changes in LDH levels in the cell culture supernatant of PC-3 cells after different treatments. The expression levels of IL-1β and IL-18 in the cell culture supernatants of PC-3 cells after group treatments were assessed using the ELISA method. Each group was repeated three times.

In vivo Cytotoxicity of DOX-HA/ZnPc-bMSN Nanocomposites

To evaluate in vivo toxicity of different drugs through hemolysis assay. The 4% red blood cell suspension was extracted from the blood of BALB/c mice. Five test tubes were taken, each containing Triton X-100 (1%), bMSN NPs, DOX-HA/ZnPc-bMSN nanocomposites, DOX+ZnPc, and DMSO, respectively. Blood samples were then added to each test tube, mixed gently, and incubated at 37°C for 2 hours. After incubation, the liquids from each test tube were centrifuged at 13,000 rpm for 15 minutes. The supernatant was discarded, and an equal volume of distilled water was added to each tube, followed by incubation at 37°C for 4 hours. The absorbance of each sample was measured at 540 nm using the microplate reader, and the hemolysis rate was calculated.

For the acute toxicity assay, since ZnPc exhibits no dark toxicity,[32] BALB/c mice were randomly divided into two groups: the DOX-HA/ZnPc-bMSN nanocomposites group and the DOX group. The day before treatment, the mice were fasted and water-deprived overnight. On the following day, different doses of DOX-HA/ZnPc-bMSN nanocomposites and DOX were administered via tail vein injection. The mortality of the mice was recorded over 14 days post-administration, and the LD50 of DOX-HA/ZnPc-bMSN nanocomposites and DOX was calculated using Probit regression analysis with SPSS software. Subsequently, the effects of DOX-HA/ZnPc-bMSN nanocomposites and their components (DOX and ZnPc) on damage to major organs and blood biochemical indicators in mice were further investigated. 200 μL of DOX-HA/ZnPc-bMSN nanocomposites and a solution of DOX+ZnPc at the same drug concentration were injected into the tail vein. ZnPc at a dose of 50 mg/kg and DOX at 5 mg/kg. The mortality within 2 weeks was recorded. For pathology, blood biochemistry, and inflammation tests, 12 female BALB/c mice were used. After being fed for 3 days, the mice were randomly divided into 4 groups. The injection method was consistent with the aforementioned acute toxicity dosing procedure. 14 days after injection, blood samples from 3 BALB/c mice in each group were collected to measure their major blood biochemistry indices and inflammation marker concentrations like TNF-α and IL-6. The BALB/c mice were then euthanized, and their hearts, livers, lungs, and kidneys were collected for histopathological analysis. All animal experiments in this work were authorized by the Laboratory Animal Administration Committee of Xi'an Medical University. The protocols for animal experiments followed the Guidelines for the Use and Care of Experimental Animals at Xi'an Medical University. The Animal Ethics Approved Document Number was XYLS2022188.

In vivo Distribution and Target Delivery of Nanocomposites

Male BALB/c-nu/nu mice (4 weeks of age) were fed for one week, each mouse was subcutaneously injected with 100 μL of PC-3 cells (5×10^5/mL). After 1 week, the tumors were measured, and when the tumors reached an adequate size, the model animals were used for further in vivo investigations. When the tumors reached an appropriate size, two tumor-bearing mice with the same tumor size were selected for the in vivo distribution experiment of nanocomposites. One mouse received an intravenous injection of 200 μL of DOX-HA/IR-780-bMSN nanocomposites, while the other mouse was intravenously injected with free IR-780. After injection, the mice were observed by the in vivo imaging system (IVIS, Perkin-Elmer, Waltham, MA, USA) with the excitation wavelength set at 660 nm. During imaging, the mice were anesthetized with isoflurane. Fluorescent images of the mice were captured at 0 h, 6 h, 12 h, 36 h, 48 h, and 96 h post-injection. When the observations were finished, the mice were euthanized, and their hearts, livers, spleens, lungs, kidneys, and tumor tissues were collected. The fluorescence signals in each organ were detected using the IVIS imaging system under the same parameters, and the biological distribution of DOX-HA/IR-780-bMSN nanocomposites in the mouse organs was analyzed.

In vivo Tumor Suppression of DOX-HA/ZnPc-bMSN Nanocomposites

Thirty tumor-bearing mice were randomly divided into 5 groups for the evaluation of the in vivo antitumor effects. Each group was injected with 200 μL of ZnPc, DOX, ZnPc+DOX, and DOX-HA/ZnPc-bMSN nanocomposites, while the control group was injected with the same volume of saline. The ZnPc at a dosage of 2 mg/kg and DOX at a dosage of 0.2 mg/kg. Injections were administered 3 times per week, and on the day after injection, the mice were exposed to 660 nm laser (0.05 W/cm^2) for 2 hours while anesthetized with isoflurane. The tumor volumes and body weights were recorded continuously. After 30 days, the mice were euthanized, and tumor tissues were collected to measure their size and weight. Subsequently, tumor tissues from each group were embedded in paraffin for H&E staining and TUNEL staining. Additionally, another five PCa xenograft mice were subjected to the same treatment intervention. Tumor tissues were collected 6 hours post-treatment to prepare fresh frozen sections. The levels of ROS in the tumor tissue were assessed using the ROS detection kit according to the instructions, where blue fluorescence indicates the cell nucleus and red fluorescence indicates ROS-positive expression.

Statistical Analysis

Statistical analysis was conducted using GraphPad Prism software. Data are presented as mean ± SD and were obtained from at least 3 independent experiments. Analysis of variance was used to assess the significance of differences between means. A p-value < 0.05 indicated a statistically significant difference between the compared data.

Results and Discussion

Preparation and Characteristics of DOX-HA/ZnPc-bMSN Nanocomposites

As illustrated in Scheme 1, ZnPc is encapsulated within the pores of bMSN NPs to form a positively charged PDT module bMSN@ZnPc NPs. Meanwhile, HA loaded with DOX forms a negatively charged CT module DOX-HA NPs. Subsequently, DOX-HA NPs are adsorbed onto the surface of bMSN@ZnPc NPs via electrostatic interactions, ultimately resulting in the formation of blackberry-like DOX-HA/ZnPc-bMSN nanocomposites. The double-layered nanocomposites effectively address the challenge of achieving high co-loading efficiency for both DOX and ZnPc, despite their distinct water solubility. These nanocomposites allow for precise tuning of drug concentrations and ratios, enabling their adaptation to diverse dual-drug synergistic therapy regimens. Through structural optimization of the nanocomposites, maximal therapeutic efficacy can be attained.[33,34] The encapsulation efficiency of ZnPc and DOX in DOX-HA/ZnPc-bMSN nanocomposites was 95.2 ± 2.6% and 85.8 ± 4.7%, respectively, with a drug loading content of 10.2 ± 1.6% and 1.4 ± 0.5%, representing a 10.9-fold and 1.7-fold increase, respectively, compared to the TNP/DOX/ZnPc system developed by Huang et al.[18] HA, a ligand for the cluster determinant 44 (CD44) receptor highly expressed in various tumors, endows DOX-HA/ZnPc-bMSN nanocomposites with tumor-targeting properties.[35] After HA-mediated targeting and entry into tumor cells, the DOX located on the surface of the nanocomposites is released first, followed by the release of ZnPc located within the pores. DOX can not only interfere with DNA replication and transcription to inhibit the proliferation of tumor cells, but also trigger tumor cell apoptosis and pyroptosis through oxidative stress.[36,37] Under 660 nm laser irradiation, ZnPc can generate ROS, which can induce tumor cell apoptosis and pyroptosis, exerting therapeutic effects. Thus, the DOX-HA/ZnPc-bMSN nanocomposites are able to precisely target tumor cells, combining DOX and ZnPc to exert antitumor effects through different mechanisms, resulting in highly efficient synergistic antitumor activity, while significantly reducing drug dosage and its associated toxicity.

Figure 1A shows the TEM images of DOX-HA NPs, bMSN NPs, and DOX-HA/ZnPc-bMSN nanocomposites. DOX-HA NPs showed analogous spherical shapes and approximately uniform sizes (14.9 ± 6.5 nm). bMSN NPs were mesoporous, exhibited good dispersibility, and possessed a uniform particle size, with an average diameter of 63.9 ± 8.6 nm. Furthermore, Malvern particle size analyzer measurements showed that the average hydrodynamic diameter of DOX-HA NPs was 25.37 nm (Supplementary Figure 1) and that of bMSN NPs was 72.03 nm (Figure 1B), while the zeta potential of DOX-HA NPs and bMSN NPs was −21.4 mV (Supplementary Figure 2) and +29.7 mV (Figure 1C), respectively. DOX-HA/ZnPc-bMSN nanocomposites exhibit a regular blackberry-like structure (Figure 1A), with an average hydrodynamic diameter of 107.8 nm (Figure 1B), which is slightly larger than the particle size shown in the

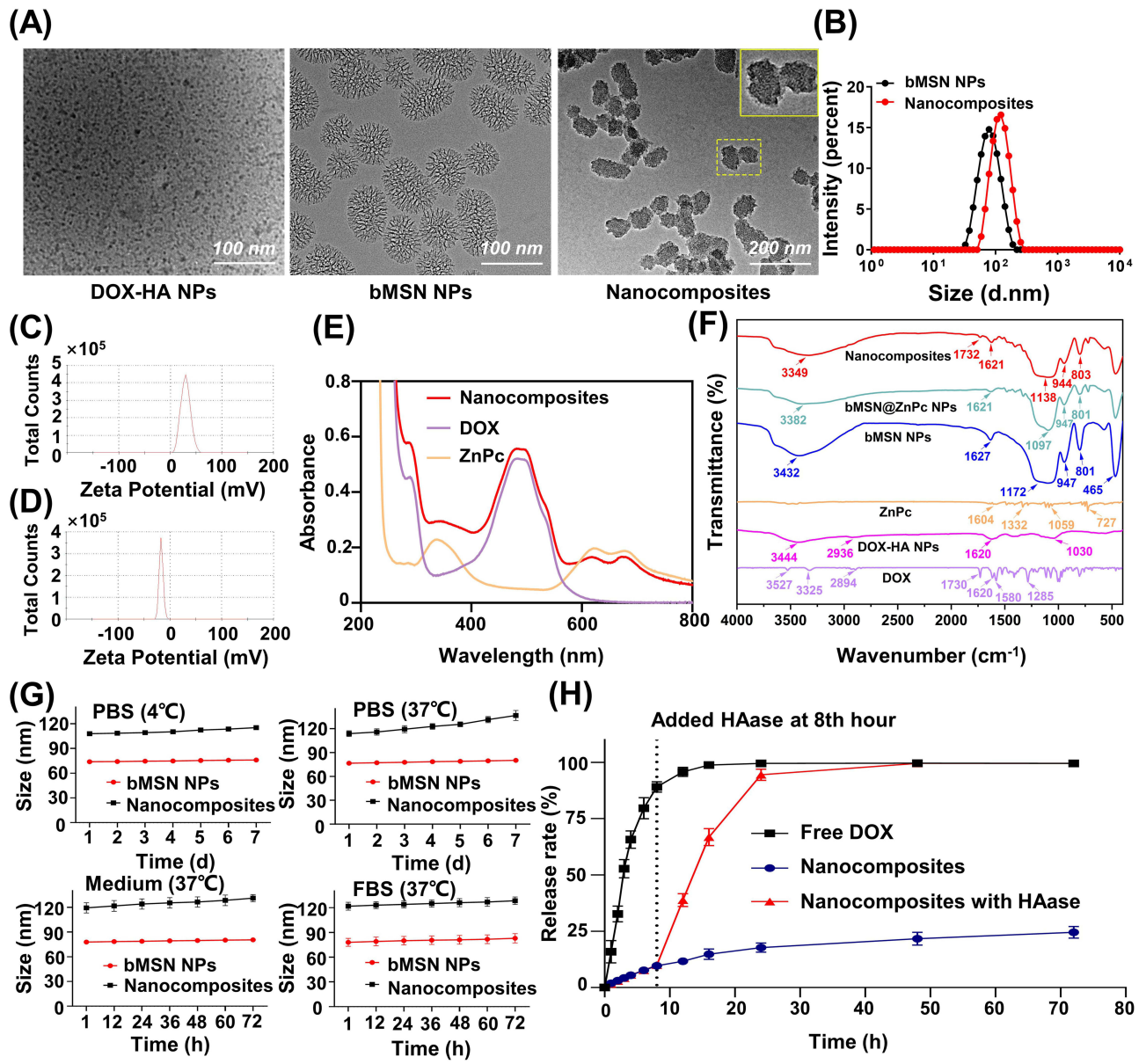

Figure 1 Characterization of DOX-HA NPs, bMSN NPs, and DOX-HA/ZnPc-bMSN nanocomposites. (**A**) TEM image of DOX-HA NPs (scale bar, 100 nm), bMSN NPs (scale bar, 100 nm), and DOX-HA/ZnPc-bMSN nanocomposites (scale bar, 200 nm). (**B**) Particle size distribution of bMSN NPs and DOX-HA/ZnPc-bMSN nanocomposites. (**C**) Zeta potential of bMSN NPs. (**D**) Zeta potential of DOX-HA/ZnPc-bMSN nanocomposites. (**E**) Absorbance spectrum of DOX-HA/ZnPc-bMSN nanocomposites. (**F**) The IR spectra analysis of DOX, DOX-HA NPs, ZnPc, bMSN NPs, bMSN@ZnPc NPs, and DOX-HA/ZnPc-bMSN nanocomposites. (**G**) Particle size changes of DOX-HA/ZnPc-bMSN nanocomposites at different temperatures and in different solvents. (**H**) In vitro release of free DOX, DOX-HA/ZnPc-bMSN nanocomposites, and HAase-containing DOX-HA/ZnPc-bMSN nanocomposites. Data presented as mean ± standard deviation (n = 3).

TEM image (80.3 ± 5.7 nm). This discrepancy was attributed to the hydration layer thickness added by the HA layer, causing the hydrodynamic diameter of the nanodrug carrier complex to be larger than that detected by transmission electron microscopy. Furthermore, the nanoparticle composite exhibited a uniform particle size distribution, with sizes around 100 nm, which allowed for effective accumulation at the tumor region through the EPR effects.[38] Notably, the zeta potential of DOX-HA/ZnPc-bMSN nanocomposites was −16.7 mV (Figure 1D), and this change in zeta potential confirms that the construction of the nanocomposites was an encapsulation process.

The FTIR was used to characterize DOX-HA/ZnPc-bMSN nanocomposites by identifying functional groups. Figure 1F displays the obtained spectra. For pure DOX, the absorption peaks observed at 3527 cm^{-1} and 3325 cm^{-1}, located in the higher wavenumber region, are assigned to N-H and O-H stretching vibrations, respectively. The

absorption at 2894 cm^{-1} arises from C-H stretching vibrations, specifically involving aromatic or alkyl hydrogen atoms. A distinct peak at 1730 cm^{-1} is indicative of C=O stretching vibrations, serving as a characteristic marker for the ketone functional group within the DOX. Additionally, the peaks at 1620 cm^{-1} and 1580 cm^{-1} are assigned to the stretching vibrations of the benzene ring C=C bonds and N-H bending vibrations, respectively. Furthermore, the C-O-C stretching vibration is identified by the band at 1285 cm^{-1}.[39] In the infrared spectrum of DOX-HA NPs, only the characteristic absorption peaks of HA are clearly observed. The broad absorption band at 3444 cm^{-1} corresponds to the O-H stretching vibration in HA, while the weaker absorption band at 2936 cm^{-1} is attributed to C-H stretching vibrations, primarily from the CH_2 and CH_3 groups in HA. The broad absorption peak appearing near 1620 cm^{-1} is characteristic of C=O stretching vibrations, which may be related to either the carboxyl groups of HA or the ketone groups of DOX. The peak at 1030 cm^{-1} arises from the C-O bond vibrations in the glucosamine and glucuronic acid backbone of HA. Notably, the characteristic absorption peaks of DOX are not distinctly observed. This phenomenon could be attributed to the fact that HA and DOX are primarily bound through electrostatic interactions, with HA encapsulating the DOX molecules, thereby masking the infrared signals of DOX. These results collectively indicate that DOX is effectively encapsulated within HA.[40] ZnPc contains multiple aromatic ring structures, with the 1604 cm^{-1} peak corresponding to the C=C stretching vibration of the aromatic rings. The 1332 cm^{-1} peak is attributed to the C-N stretching vibration, while the 1059 cm^{-1} peak arises from either C-N bending vibration or C-H bending vibration. Additionally, the vibrational peak at 727 cm^{-1} represents the characteristic frequency of the Zn-N bond.[41] In the infrared spectrum of bMSN NPs, the broad and strong absorption peak at 3432 cm^{-1} can be attributed to the stretching vibration of Si-OH. The peak at 1627 cm^{-1} corresponds to the C=O stretching vibration in COOH groups. The absorption peak at 1172 cm^{-1} corresponds to the stretching vibration of the Si-O-Si bond, while the peaks at 947 cm^{-1}, 801 cm^{-1}, and 465 cm^{-1} are all attributed to the bending vibrations of the Si-O-Si bond. These peaks collectively reflect the characteristic features of the bMSN NPs.[42] Compared to pure ZnPc, the bMSN@ZnPc NPs demonstrate a distinct Si-O vibrational peak at 1097 cm^{-1}, which originates from the silica framework of bMSN NPs. The absorption peak at 1621 cm^{-1} is attributed to the C=C stretching vibration, highlighting the aromatic ring structure within the ZnPc molecule. Furthermore, the broad absorption band observed at 3382 cm^{-1} suggests the formation of hydrogen bonding interactions between ZnPc and bMSN NPs. These infrared spectral features collectively provide strong evidence for the successful preparation of the bMSN@ZnPc NPs. It is noteworthy that the characteristic peaks of the raw materials are all visible in the infrared spectrum of the DOX-HA/ZnPc-bMSN nanocomposites, while the intensity and position of some peaks have changed. For instance, the O-H stretching vibration peak originally located at 3444 cm^{-1} has shifted to 3349 cm^{-1}, accompanied by peak broadening and enhanced intensity. This shift is primarily attributed to the intermolecular interactions between DOX-HA NPs, ZnPc, and bMSN NPs. These spectral changes, along with the presence of all relevant characteristic peaks, collectively provide strong evidence for the successful preparation of the DOX-HA/ZnPc-bMSN nanocomposites.

Absorbance spectrum analysis (Figure 1E) revealed that DOX-HA/ZnPc-bMSN nanocomposites exhibited significant absorption peaks at 490 nm and 620–680 nm, indicating that the loading of ZnPc onto bMSN NPs did not alter its properties, thereby preserving the PDT efficacy of nanocomposites. Additionally, as shown in Supplementary Figure 3, the absorbance increased proportionally with the concentration of DOX-HA/ZnPc-bMSN nanocomposites. To evaluate the stability of the nanocomposites, the particle sizes of DOX-HA/ZnPc-bMSN nanocomposites were measured under different temperatures and media conditions. As illustrated in Figure 1G, both bMSN NPs and DOX-HA/ZnPc-bMSN nanocomposites demonstrated excellent stability in PBS at 4°C, PBS at 37°C, DMEM at 37°C, and FBS at 37°C, with no particle size change exceeding 10%. Additionally, the DOX-HA/ZnPc-bMSN nanocomposites were stored in the dark at 4°C for 12 weeks, their particle size remained almost unchanged (Supplementary Figure 4). These findings indicate that DOX-HA/ZnPc-bMSN nanocomposites exhibit excellent stability, making them suitable for further research. Figure 1H depicts the DOX release profile from DOX-HA/ZnPc-bMSN nanocomposites. In the free DOX group, DOX exhibited rapid and continuous release, reaching 95.8% within 12 hours, after which the release plateaued, which is consistent with the findings reported by Ma et al.[43] In contrast, the DOX-HA/ZnPc-bMSN nanocomposites demonstrated a sustained release profile, with only 11.7% released at 12 hours and 24.5% at 72 hours. The presence of HAase significantly modulated DOX release. Prior to HAase addition, DOX release remained steady. However, upon HAase addition after 8 hours, DOX was rapidly released, achieving 94.5% at 24 hours and 99.5% at 72 hours. The release trend of ZnPc was

generally similar to that of DOX (Supplementary Figure 5), but its release curve was more gradual, with a release rate of 67.5% at 12 hours and a maximum release rate of 69.9% at 72 hours, which was significantly lower than that of DOX. This is consistent with the findings reported by Wang et al.[19] The release rate of ZnPc from the DOX-HA/ZnPc-bMSN nanocomposites was also lower than that of DOX, with 4.7% released at 12 hours and 8.2% at 72 hours. Following the addition of HAase (at 8 hours), DOX in the DOX-HA/ZnPc-bMSN nanocomposites was released first, followed by a rapid release of ZnPc at around 10 hours, reaching a release rate of 61.7% at 24 hours and 69.7% at 72 hours. This phenomenon may be attributed to the hydrophobic nature of ZnPc, which results in both a slower release rate and a lower cumulative release amount compared to DOX. These results demonstrate that free DOX and ZnPc achieve rapid release, while the nanocomposites enable controlled and sustained release. The accelerated release in the presence of HAase suggests that the nanocomposites can achieve on-demand drug release in vivo, making it a promising candidate for antitumor research.

Cell Internalization Evaluation of DOX-HA/ZnPc-bMSN Nanocomposites

To evaluate the cellular uptake behavior of PC-3 cells toward nanocomposites, coumarin 6 was loaded into the pores of bMSN NPs as a substitute for ZnPc. As shown in Figure 2A, the fluorescence signals of coumarin 6 (green) and DOX (red) were primarily localized in the cytoplasm after 1 hour. Over time, the fluorescence intensity of coumarin 6 in the cytoplasm gradually increased, while the red fluorescence signal of DOX shifted from the cytoplasm to the nucleus, with its intensity continuously rising. Figure 2B and C illustrate that the ratio of DOX fluorescence intensity in the nucleus to that in the cytoplasm progressively increased, whereas the ratio of coumarin 6 fluorescence intensity in the nucleus to the cytoplasm gradually decreased. These results indicate that DOX was gradually translocated into the nucleus, while coumarin 6 remained predominantly enriched in the cytoplasm. This demonstrates that DOX-HA/ZnPc-bMSN nanocomposites can be effectively internalized by PC-3 cells, enabling efficient drug and photosensitizer delivery, achieving stepwise release, and laying the groundwork for in vivo tumor synergistic therapy.

To further assess the targeting capability of DOX-HA/ZnPc-bMSN nanocomposites, in vitro targeting experiments were conducted in PC-3 cells. As shown in Figure 2D, the fluorescence intensity in the HA-blocking group was significantly lower than that in the control group. Figure 2E and F further reveal that the ratios of DOX and coumarin 6 fluorescence intensity in the nucleus to the cytoplasm were lower in the HA-blocking group compared to the control group, suggesting that HA competitively inhibits the cellular internalization of HA-coated DOX-HA/ZnPc-bMSN nanocomposites. Therefore, the targeting capability of DOX-HA/ZnPc-bMSN nanocomposites primarily relies on HA, and their effective targeting ensures efficient drug delivery in vivo.

In vitro Cytotoxicity of DOX-HA/ZnPc-bMSN Nanocomposites

The low cytotoxicity and effective in vitro antitumor activity of DOX-HA/ZnPc-bMSN nanocomposites are essential prerequisites for their in vivo application. In this study, the in vitro cytotoxicity of DOX-HA/ZnPc-bMSN nanocomposites was evaluated using two normal cell lines (HT-22, HUVEC) and one PCa cell line (PC-3). As shown in Figure 3A–C, ZnPc exhibited no significant cytotoxicity without laser irradiation, while the toxicity of DOX and DOX-HA/ZnPc-bMSN nanocomposites increased with concentration augment. Notably, DOX-HA/ZnPc-bMSN nanocomposites demonstrated a cell inhibition effect comparable to that of DOX alone, indicating that they retained DOX's cytotoxicity and effectively inhibited cell proliferation. Next, the viability of PC-3 cells treated with DOX-HA/ZnPc-bMSN nanocomposites under laser irradiation was assessed. As shown in Figure 3E, in all laser-irradiated groups, the cytotoxicity of DOX-HA/ZnPc-bMSN nanocomposites was concentration-dependent, with cell viability decreasing as the nanocomposites concentration increased. At the highest concentration (83.3 μg/mL), PC-3 cell viability dropped to approximately 10%. In contrast, without laser irradiation, even at the highest concentration of DOX-HA/ZnPc-bMSN nanocomposites (83.3 μg/mL), PC-3 cell viability remained around 40%. These results demonstrate that the combination of DOX-HA/ZnPc-bMSN nanocomposites and laser irradiation significantly enhances tumor cell inhibition.

The colony formation assay was used to evaluate the proliferative capacity of PC-3 cells under different treatments. As shown in Figure 3F, the control group exhibited the highest colony density, while the ZnPc+laser and DOX groups showed significantly fewer colonies. The DOX+ZnPc+laser group had even fewer colonies, and the DOX-HA/ZnPc-

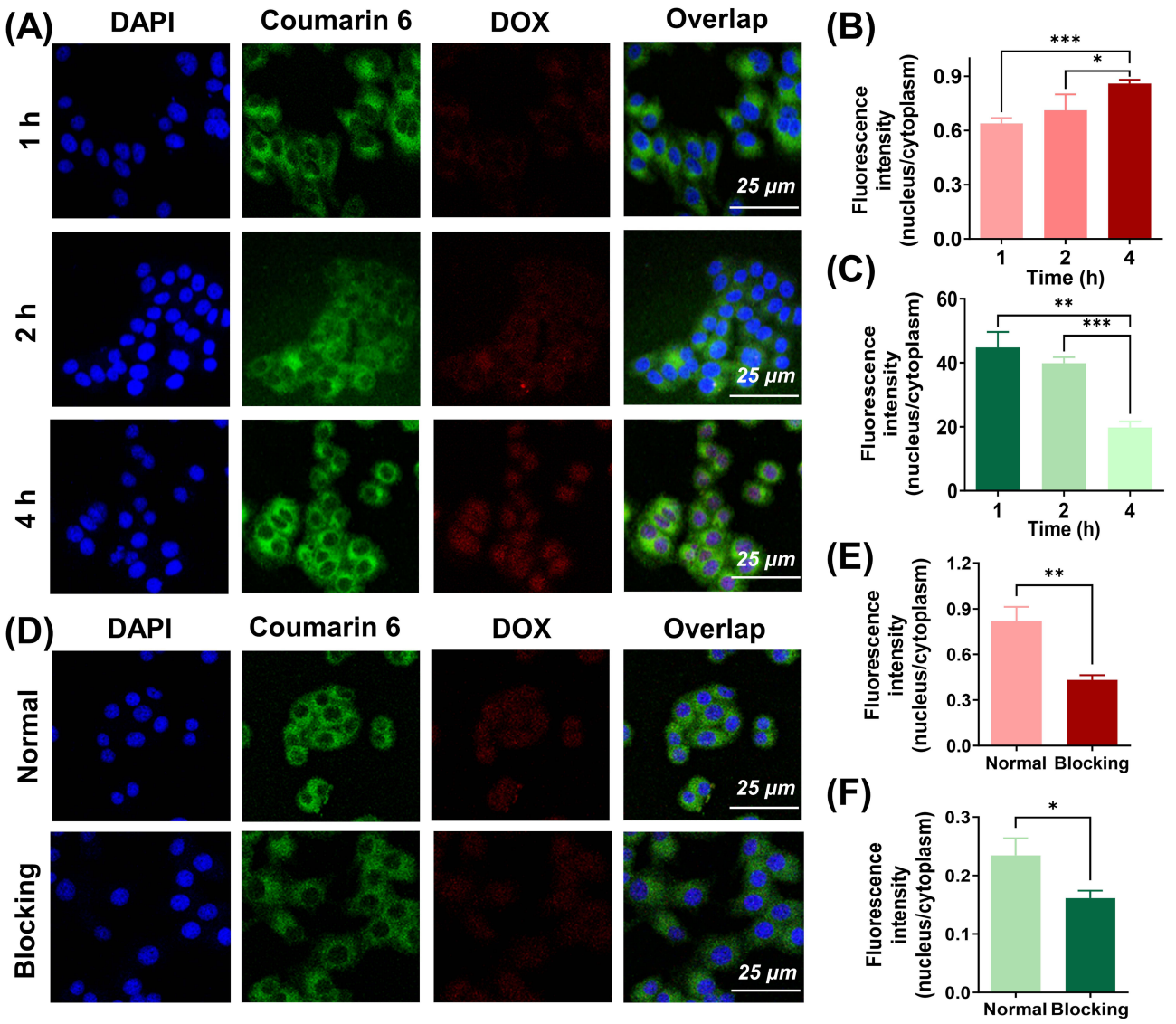

Figure 2 Cell internalization evaluation of DOX-HA/ZnPc-bMSN nanocomposites. (**A**) Fluorescence microscopic images of PC-3 cells incubated with fluorescently labeled DOX-HA/ZnPc-bMSN nanocomposites for 1 h, 2 h, and 4 h. (**B**) Ratio of fluorescence intensity of DOX in the nucleus to the cytoplasm. (**C**) Ratio of fluorescence intensity of coumarin 6 in the nucleus to the cytoplasm. (**D**) Fluorescence microscopic images of internalized DOX-HA/ZnPc-bMSN nanocomposites with or without HA blocking. (**E**) Ratio of fluorescence intensity of DOX in the nucleus to the cytoplasm after internalization of DOX-HA/ZnPc-bMSN nanocomposites with or without HA blocking. (**F**) Ratio of fluorescence intensity of coumarin 6 in the nucleus to the cytoplasm after internalization of DOX-HA/ZnPc-bMSN nanocomposites with or without HA blocking. Scale bar, 25 μm. Error bars represent the standard deviation of the mean. *$p < 0.05$, **$p < 0.01$, ***$p < 0.001$.

bMSN nanocomposites+laser group displayed the fewest colonies, highlighting the potent anti-proliferative effect of the nanocomposites combined with laser irradiation. Figure 3G presents the quantitative analysis of colony counts using Image J software, which aligns with the visual results. Additionally, live-dead cell staining (Figure 3H) revealed that the DOX-HA/ZnPc-bMSN nanocomposites+laser group had the lowest cell survival rate. In vitro experiments, including CCK-8 assays, colony formation assays, and live/dead cell staining, consistently revealed that DOX-HA/ZnPc-bMSN nanocomposites+laser exhibited a dose-dependent and significantly enhanced inhibitory effect on the growth of PC-3 cells, surpassing all other treatment groups.

Dose-response curves (Figure 3D) were plotted to determine the IC50 values of ZnPc+laser, DOX, and DOX-HA/ZnPc-bMSN nanocomposites+laser (Supplementary Table 1), the CI for DOX-HA/ZnPc-bMSN nanocomposites+laser was calculated to be as low as 0.26 (range: 0.26–0.52). A CI value below 1.0 typically indicates a synergistic effect, with values under 0.8 reflecting a highly pronounced synergy.[44] These results underscore the exceptional synergistic antitumor

https://doi.org/10.2147/IJN.S530041

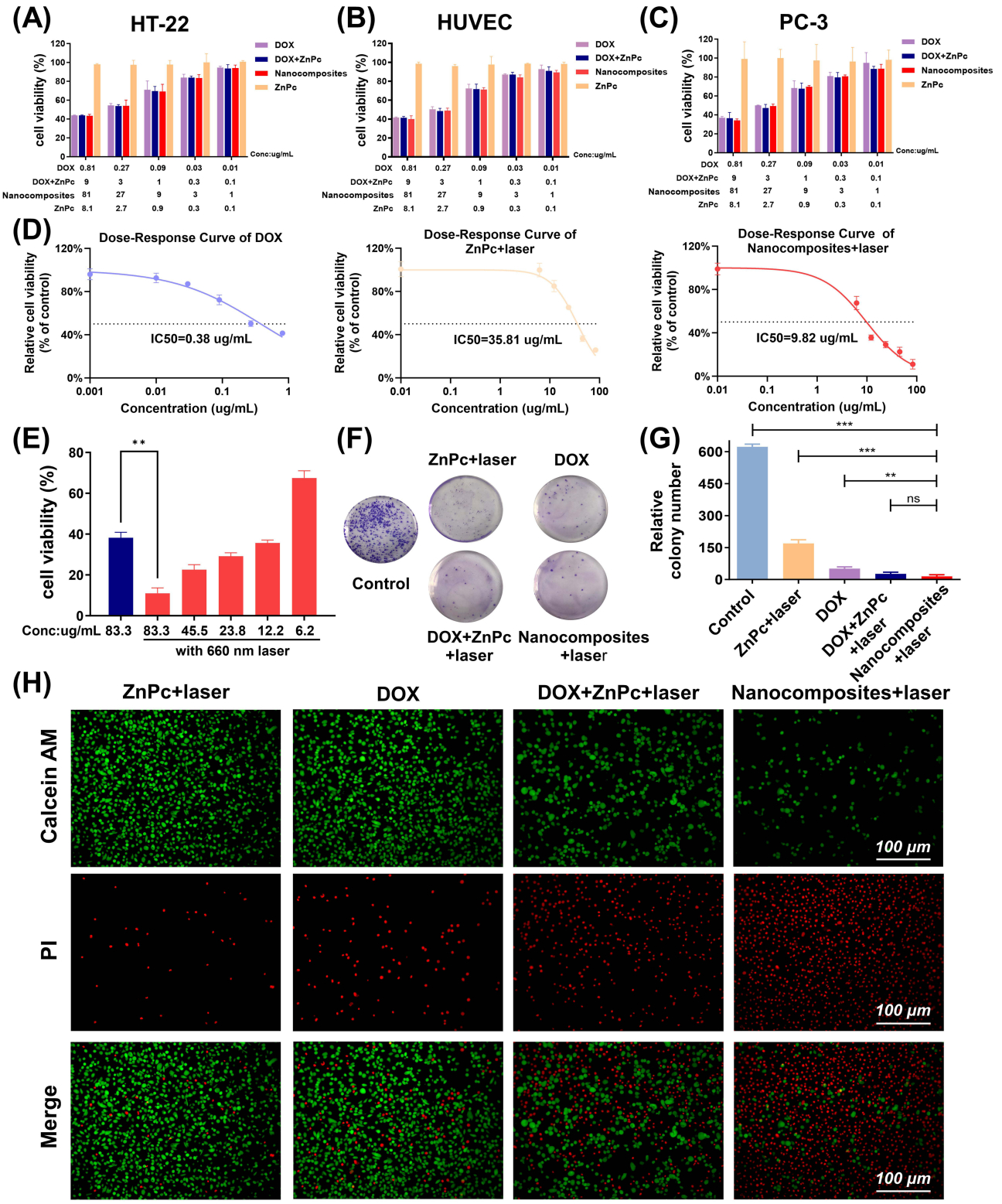

Figure 3 In vitro toxicity of DOX-HA/ZnPc-bMSN nanocomposites. (**A**–**C**) Cytotoxicity test results of DOX-HA/ZnPc-bMSN nanocomposites on cell lines including HT-22, HUVEC, and PC-3. (**D**) Dose-response curves of DOX, ZnPc+laser, and DOX-HA/ZnPc-bMSN nanocomposites+laser on the PC-3 cell line. (**E**) Cell survival rate of PC-3 cells after laser treatment with DOX-HA/ZnPc-bMSN nanocomposites. (**F**) Results of the clone formation assay of PC-3 cells after treatments. (**G**) Quantitative data of clone formation assay of PC-3 cells after treatments. (**H**) Fluorescence microscopic images of live-dead cell staining results of PC-3 cells after treatments. Scale bar, 100 μm. Error bars represent the standard deviation of the mean. $^{**}p < 0.01$, $^{***}p < 0.001$.

Abbreviation: ns, not significant.

efficacy of DOX-HA/ZnPc-bMSN nanocomposites. Furthermore, their performance markedly outperforms that of TPCI/DOX@Lipo (CI ≥ 0.45) synthesized by Wang et al[45] and DOX-ZnPc-micelles (CI ≥ 0.5) developed by Gao et al.[46]

Inhibiting Efficacy of DOX-HA/ZnPc-bMSN Nanocomposites on the Proliferation of PC-3 Cells

The ROS staining experiment was conducted to evaluate the in vitro photodynamic effect of DOX-HA/ZnPc-bMSN nanocomposites. DCFH-DA, a widely used fluorescent probe for detecting singlet oxygen, exhibits fluorescence intensity proportional to intracellular ROS levels. Previous studies have shown that both DOX and PDT can promote ROS generation, leading to oxidative damage and apoptosis in tumor cells.[21,47] After treating PC-3 cells with different approaches, DCFH-DA staining revealed that the fluorescence signal intensity was weakest in the DOX group and strongest in the DOX-HA/ZnPc-bMSN nanocomposites+laser group (Figure 4A). Quantitative analysis using Image J software demonstrated that DOX-HA/ZnPc-bMSN nanocomposites increased ROS production by 2.2-fold and 4.1-fold compared to free ZnPc and free DOX, respectively, while the DOX+ZnPc+laser group showed a 1.6-fold increase (Figure 4I). Flow cytometry was further employed to assess PC-3 cell apoptosis under different treatments. As shown in Figure 4B, the apoptosis rates in the DOX, ZnPc+laser, DOX+ZnPc+laser, and DOX-HA/ZnPc-bMSN nanocomposites +laser groups were 13.5%, 16.1%, 36.1%, and 44.1%, respectively. The apoptosis rate in the DOX-HA/ZnPc-bMSN nanocomposites+laser group was 3.2-fold and 2.7-fold higher than in the DOX and ZnPc+laser groups, respectively, and 1.2-fold higher than in the DOX+ZnPc+laser group. Moreover, it was 1.3-fold higher than the apoptosis rate (32.8%) achieved by the GNS@IR820/DTX-CD133 synergistic photothermal/photodynamic/chemotherapy nanoplatform developed by Tan et al.[48] These results indicate that the combination of PDT and CT mediated by DOX-HA/ZnPc-bMSN nanocomposites significantly enhances intracellular ROS levels, effectively inducing apoptosis and inhibiting the proliferation of PC-3 cells.

Research by Wu et al demonstrated that increased ROS production during PDT can induce pyroptosis in tumor cells.[49] Given that DOX-HA/ZnPc-bMSN nanocomposites significantly enhance ROS production in PC-3 cells, it is reasonable to speculate that they may induce pyroptosis in addition to apoptosis. Since both PI staining[26] and TUNEL assays[50] produce positive results during pyroptosis, additional experiments were undertaken to verify that DOX-HA/ZnPc-bMSN nanocomposites+laser induce pyroptosis as an antitumor mechanism. Initially, morphological changes in PC-3 cells after different treatments were observed using an optical microscope (Figure 4C). While the DOX and ZnPc +laser groups showed no significant morphological changes, the DOX+ZnPc+laser group exhibited cell swelling without clear pyroptosis characteristics. In contrast, cells in the DOX-HA/ZnPc-bMSN nanocomposites+laser group lost their adherent morphology, becoming round and significantly swollen, with some cell membranes forming “balloon-like” protrusions and partial detachment. These typical pyroptotic characteristic changes suggest that DOX-HA/ZnPc-bMSN nanocomposites may induce pyroptosis in PC-3 cells.

Numerous studies have identified caspase-1 as a pivotal regulator of PDT-induced pyroptosis in tumor cells.[51,52] To further validate the hypothesis, we employed Western blotting to detect the expression of cleaved caspase-1 and cleaved N-terminal GSDMD in PC-3 cells under different treatments. As shown in Figure 4D, the expression of cleaved caspase-1 and cleaved N-terminal GSDMD in PC-3 cells treated with DOX or ZnPc+laser was lower than in the control group. In contrast, the DOX+ZnPc+laser group exhibited slightly higher expression levels of these proteins compared to the control. Notably, the DOX-HA/ZnPc-bMSN nanocomposites+laser group showed a significant increase in the expression of cleaved caspase-1 and cleaved N-terminal GSDMD, with statistically significant differences (Figure 4E). Furthermore, a pivotal step in pyroptosis involves the formation of plasma membrane pores by pyroptosis execution proteins, facilitating the release of LDH and inflammatory cytokines such as IL-1β and IL-18 into the extracellular space.[53] Accordingly, we quantified LDH levels and the expression of inflammatory markers IL-1β and IL-18 in the supernatant of PC-3 cells after various treatments. The results revealed that the DOX and ZnPc+laser groups showed only a slight increase in LDH levels, with negligible concentrations of IL-1β and IL-18. In contrast, the DOX-HA/ZnPc-bMSN nanocomposites+laser group exhibited the highest concentrations of LDH, IL-1β, and IL-18 in the supernatant (Figure 4F–H), with levels 2.1-fold, 4.2-fold, and 7.8-fold higher, respectively, than those in the DOX+ZnPc+laser

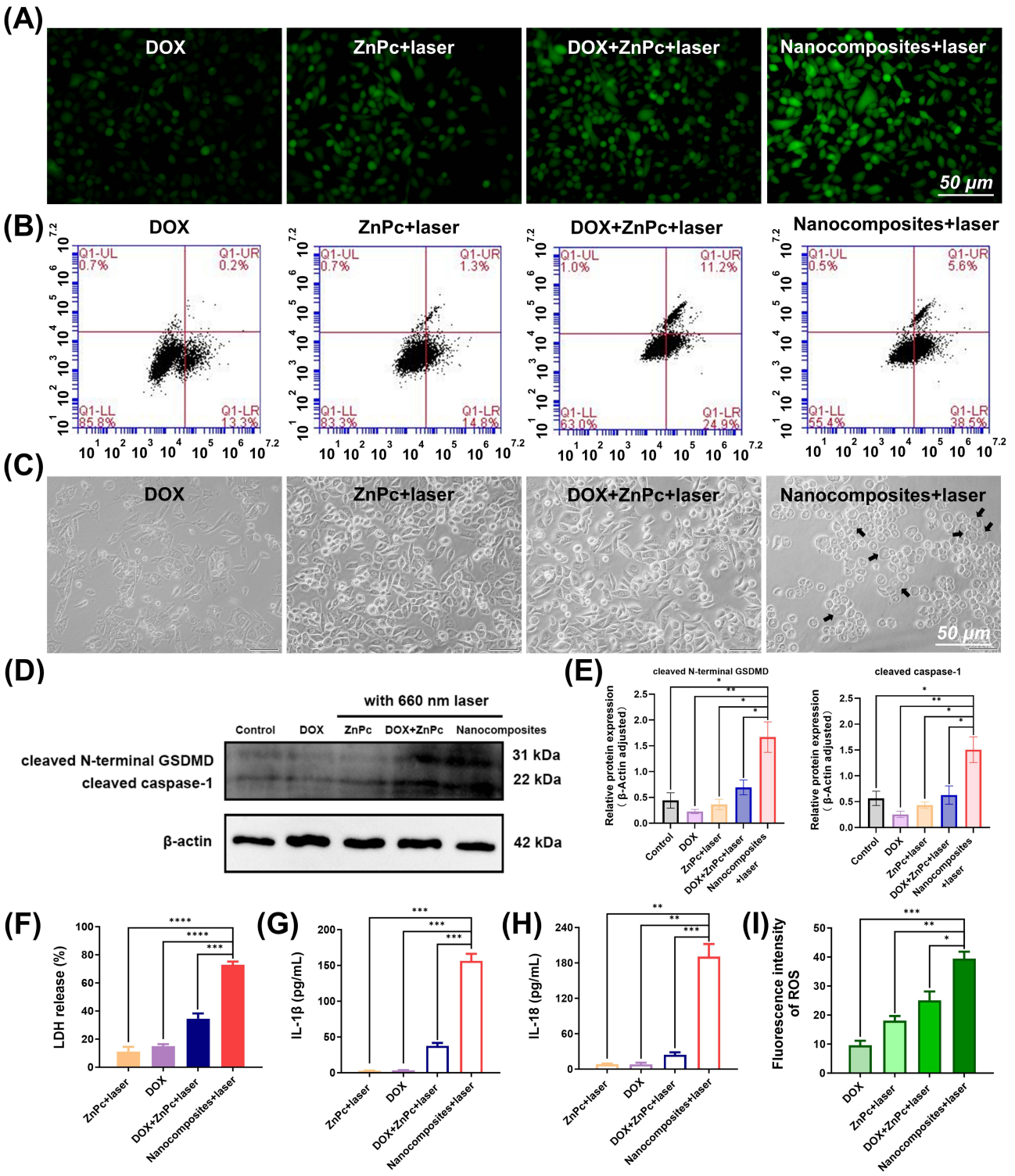

Figure 4 Inhibiting efficacy of DOX-HA/ZnPc-bMSN nanocomposites on the proliferation of PC-3 cells. (**A**) Fluorescence microscopic images of intracellular ROS generation in PC-3 cells after treatments. Scale bar, 50 μm. (**B**) Flow cytometry analysis of apoptosis in PC-3 cells after treatments. (**C**) Images of PC-3 cells after treatments. Black allows indicated pyroptotic PC-3 cells with a damaged cell membrane or large bubbles. Scale bar, 50 μm. (**D**) Western blot experiment to detect the expression of cleaved N-terminal GSDMD and cleaved caspase-1 in PC-3 cells after treatments (n = 3). (**E**) Quantitative analysis of the expression of cleaved N-terminal GSDMD and cleaved caspase-1 in PC-3 cells after treatments (n = 3). (**F**) LDH release from PC-3 cells after treatments (n = 3). (**G**) IL-1β levels in the cell culture supernatant of PC-3 cells after treatments (n = 3). (**H**) IL-18 levels in the cell culture supernatant of PC-3 cells after treatments (n = 3). (**I**) Quantitative analysis of intracellular ROS generation fluorescence intensity in PC-3 cells after treatments. Error bars represent the standard deviation of the mean. *$p < 0.05$, **$p < 0.01$, ***$p < 0.001$, ****$p < 0.0001$.

group. These findings align with the Western blotting results, further supporting the induction of pyroptosis. In conclusion, DOX-HA/ZnPc-bMSN nanocomposites demonstrated excellent tumor-targeting capabilities and significantly enhanced ROS production by DOX and ZnPc. The elevated ROS levels not only induced apoptosis but also triggered pyroptosis in PC-3 cells via the ROS/caspase-1/GSDMD classical activation pathway. These results are consistent with the findings of Ma et al,[54] who reported that TαPcZn-PDT induces both apoptosis and pyroptosis in breast cancer MCF-7 cells, although the tumor cell inhibitory effects observed in our study are even more robust. This dual mechanism significantly improved PCD efficiency in PC-3 cells, highlighting DOX-HA/ZnPc-bMSN nanocomposites as a promising candidate for further in vivo antitumor studies.

In vivo Toxicity of DOX-HA/ZnPc-bMSN Nanocomposites

First, a direct toxicity comparison between DOX-HA/ZnPc-bMSN nanocomposites and free DOX was conducted by measuring the LD50 values. Supplementary Figure 6 shows the death rates of mice in the DOX-HA/ZnPc-bMSN nanocomposites and free DOX groups at different concentrations. The LD50 of DOX-HA/ZnPc-bMSN nanocomposites and DOX was calculated using Probit regression analysis with SPSS software. The LD50 of free DOX was 9.19 mg/kg (95% confidence interval: 6.83–11.65 mg/kg), which is consistent with the results reported in the literature (15.2 mg/kg).[55] The LD50 of DOX-HA/ZnPc-bMSN nanocomposites was 138.95 mg/kg (95% confidence interval: 115.64–165.37 mg/kg), which is 15.12 times higher than that of free DOX. The increase in LD50 indicates that DOX-HA/ZnPc-bMSN nanocomposites significantly reduce the acute toxicity of DOX in mice. Second, to further assess the potential of DOX-HA/ZnPc-bMSN nanocomposites for in vivo therapeutic applications, a comprehensive analysis of their in vivo toxicity was conducted. As shown in Figure 5A, DOX-HA/ZnPc-bMSN nanocomposites exhibited the lowest hemolysis rate at 1.9%, indicating minimal hemolytic toxicity and excellent biocompatibility. In contrast, the DOX+ZnPc group showed the highest hemolysis rate of 22.1%. After drug loading, the hemolysis rate of DOX-HA/ZnPc-bMSN nanocomposites remained low at 2.8%, confirming their safety for injection. Acute toxicity tests (Figure 5B) revealed that after 14 days, only 50% of mice in the DOX+ZnPc group survived, whereas 90% of mice in the DOX-HA/ZnPc-bMSN nanocomposites group remained alive. Additionally, mice treated with DOX-HA/ZnPc-bMSN nanocomposites exhibited steady weight gain, while those in the DOX+ZnPc group showed significantly inhibited weight growth, with a gradual decline starting from the 5th day post-intervention (Figure 5C).

To assess whether DOX-HA/ZnPc-bMSN nanocomposites induced pathological reactions in the immune system, physiology, or major organs, mice were euthanized 14 days post-treatment. Major organs and serum samples were subsequently collected for comprehensive histopathological analysis and biochemical marker assessment. Pathological analysis (Figure 5E) revealed that mice in the DOX+ZnPc group exhibited enlarged interstitial spaces and myocardial cell atrophy, accompanied by significantly elevated serum creatine kinase (CK) levels compared to the DOX-HA/ZnPc-bMSN nanocomposites group (Figure 5F), likely due to DOX-induced cardiotoxicity. In contrast, mice treated with DOX-HA/ZnPc-bMSN nanocomposites showed normal myocardial morphology with no signs of damage. Furthermore, serum levels of immune factors (TNF-α and IL-6) and liver/kidney function markers showed no significant abnormalities (Figure 5D and F). These results demonstrate that DOX-HA/ZnPc-bMSN nanocomposites exhibit excellent biocompatibility in vivo, effectively reducing DOX-induced cardiotoxicity and ensuring safety for subsequent in vivo imaging and therapeutic studies.

In vivo Distribution and Target Delivery of Nanocomposites

To evaluate the in vivo distribution of nanocomposites, PC-3 xenograft mice were utilized. The experimental group received intravenous injections of DOX-HA/IR-780-bMSN nanocomposites, while the control group was administered an equivalent volume of free IR-780. Fluorescence imaging was performed using the IVIS imaging system over a 96-hour period. As depicted in Figure 6A, fluorescence signals were observed in the tumors and other regions of the experimental group, with continuous accumulation of signals in the tumor area. The fluorescence intensity reached its peak at 36 hours and subsequently declined, with only a faint signal detectable at 96 hours. In contrast, Wang et al[56] reported that free DOX rapidly accumulates in major organs (such as the liver, spleen, lungs, and kidneys), peaking at 0.5 hours after tail vein injection, followed by a sharp decline within 24 hours. Figure 6B provides a quantitative analysis of

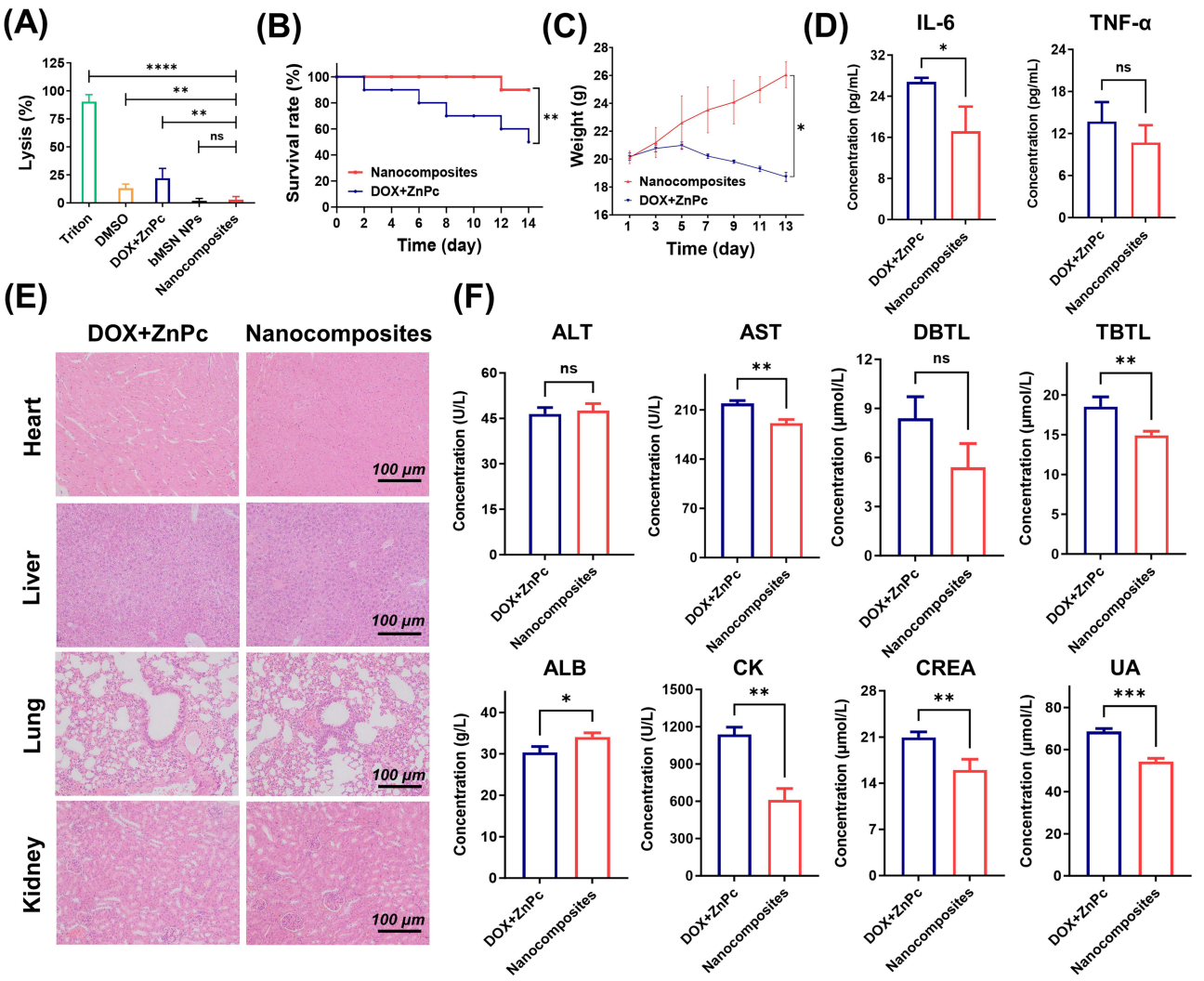

Figure 5 In vivo toxicity of DOX-HA/ZnPc-bMSN nanocomposites. (**A**) The hemolysis test results of DOX-HA/ZnPc-bMSN nanocomposites and their main components. (**B**) The in vivo acute toxicity test results of DOX+ZnPc and DOX-HA/ZnPc-bMSN nanocomposites on the BALB/c mice. (**C**) Average body weight changes of mice after treatment with DOX+ZnPc and DOX-HA/ZnPc-bMSN nanocomposites. (**D**) IL-6 and TNF-α in the blood of mice after treatment with DOX+ZnPc and DOX-HA/ZnPc-bMSN nanocomposites (n = 3). (**E**) The pathological analysis of mice after treatment with DOX+ZnPc and DOX-HA/ZnPc-bMSN nanocomposites. (**F**) Main blood biochemical indicators of mice after treatment with DOX+ZnPc and DOX-HA/ZnPc-bMSN nanocomposites (n = 3). Error bars represent the standard deviation of the mean. *$p < 0.05$, **$p < 0.01$, ***$p < 0.001$, ****$p < 0.0001$.
Abbreviation: ns, not significant.

the fluorescence intensity during the in vivo distribution experiment, corroborating the imaging results. Following the imaging process, the mice were euthanized, and tissues from the heart, liver, spleen, lung, kidney, and tumor were harvested. The fluorescence signals in these organs were measured under consistent conditions using the IVIS imaging system. As shown in Figure 6C, no fluorescence signals were detected in the organs of the control group, whereas the experimental group exhibited fluorescence signals predominantly localized in the tumor region. Figure 6D presents the quantitative analysis of fluorescence signals across the organs, revealing significantly higher fluorescence intensity in the experimental group compared to the control group, particularly in the tumor area. These results highlight that DOX-HA/ZnPc-bMSN nanocomposites significantly extend the circulation time of free DOX and ZnPc in vivo, enabling targeted and controlled drug release within tumor tissues. This facilitates the prolonged accumulation and action of the two therapeutic molecules in the tumor region, enhancing therapeutic efficacy and duration while reducing the required dosage and administration frequency, thereby minimizing drug toxicity and the risk of drug resistance.

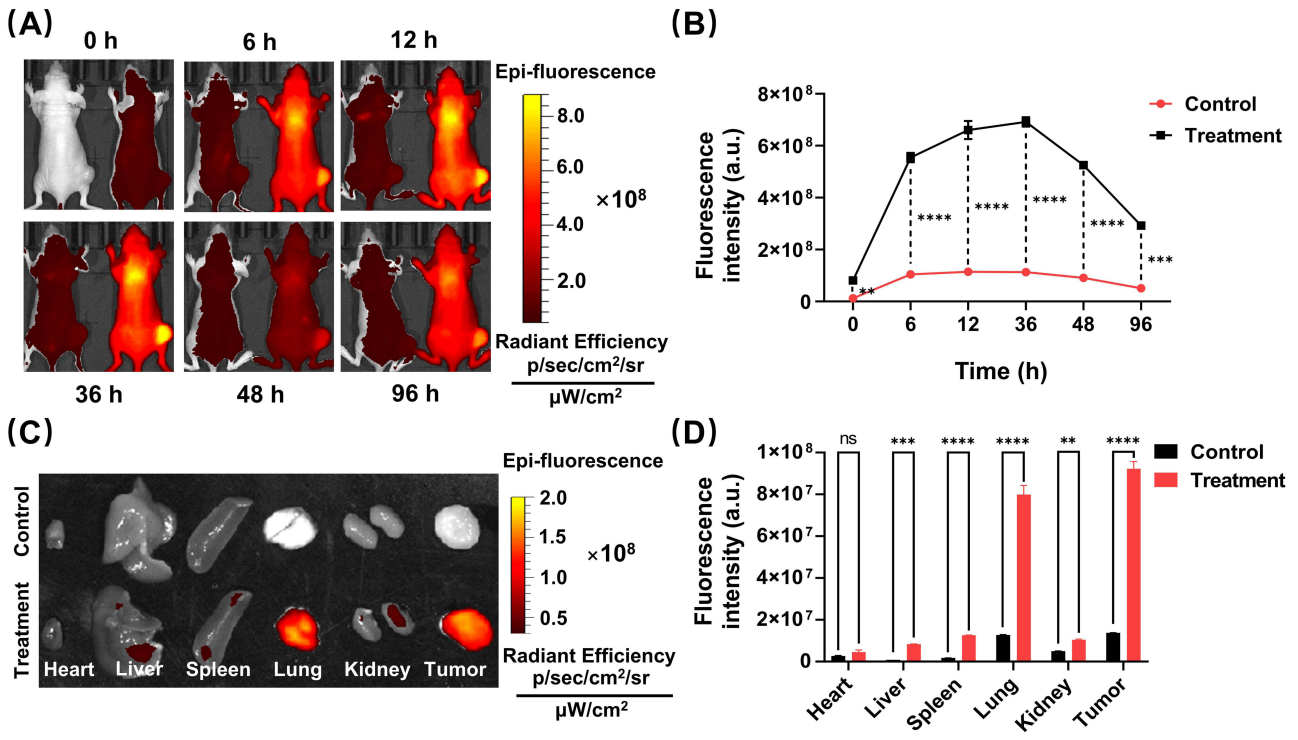

Figure 6 In vivo distribution and target delivery of nanocomposites. (**A**) The dynamic monitoring of DOX-HA/IR-780-bMSN nanocomposites in the PC-3 tumor-bearing nude mice and the fluorescent signals results of the tumor region. (**B**) Quantitative analysis of fluorescence signals in the tumor region of PC-3 tumor-bearing nude mice. (**C**) The residual fluorescent signals result in the organs and tumors of PC-3 tumor-bearing nude mice. (**D**) Quantitative analysis results of fluorescence signals in major organs and tumor tissues of PC-3 tumor-bearing nude mice. Error bars represent the standard deviation of the mean. $^{**}p < 0.01$, $^{***}p < 0.001$, $^{****}p < 0.0001$.
Abbreviation: ns, not significant.

In vivo Tumor Suppression of DOX-HA/ZnPc-bMSN Nanocomposites

To assess the in vivo antitumor efficacy of DOX-HA/ZnPc-bMSN nanocomposites, the body weight and tumor size of mice in different treatment groups were monitored over a 30-day period. Figure 7A displays representative images of excised tumors following treatment. Compared to the ZnPc+laser, DOX, and DOX+ZnPc+laser groups, the DOX-HA/ZnPc-bMSN nanocomposites+laser group exhibited the smallest tumors and the most pronounced therapeutic effect. Tumor volumes were measured at various time points, and the resulting growth curves are shown in Figure 7B and C. The saline group demonstrated the most rapid tumor growth, followed by the ZnPc+laser group. Tumor growth in the DOX and DOX+ZnPc+laser groups was relatively slower, while the DOX-HA/ZnPc-bMSN nanocomposites+laser group showed the most significant tumor growth inhibition. The tumor inhibition rate in the DOX-HA/ZnPc-bMSN nanocomposites+laser group reached 96.0%, significantly higher than that in the ZnPc+laser (27.2%), DOX (57.0%), and DOX +ZnPc+laser (62.6%) treatment groups. This outcome significantly outperforms the results obtained with TPE-APP (84.5%) developed by Xiong et al[57] and DOX/TPOR4@CB (84.17%) synthesized by Lu et al[58] Figure 7D illustrates the body weight changes of the mice throughout the experiment. A notable decline in body weight was observed in the DOX group, likely attributable to the drug's toxicity. The DOX+ZnPc+laser group exhibited greater weight loss compared to the ZnPc+laser group, further confirming the toxic effects of DOX. In contrast, the DOX-HA/ZnPc-bMSN nanocomposites+laser group showed no significant weight loss, with body weight gradually recovering after 20 days of treatment. Notably, the doses of DOX and ZnPc administered in this study were only 0.2 mg/kg and 2 mg/kg, respectively, representing a 9.1-fold reduction compared to the dose (DOX and/or ZnPC was administered at a total dose of 20 mg/kg) reported by Huang et al.[18] These results suggest that DOX-HA/ZnPc-bMSN nanocomposites effectively reduce the toxicity of DOX while enabling a synergistic combination of long-term PDT (2 hours) and CT, even at an exceptionally low dose of DOX and ZnPC.

https://doi.org/10.2147/IJN.S530041

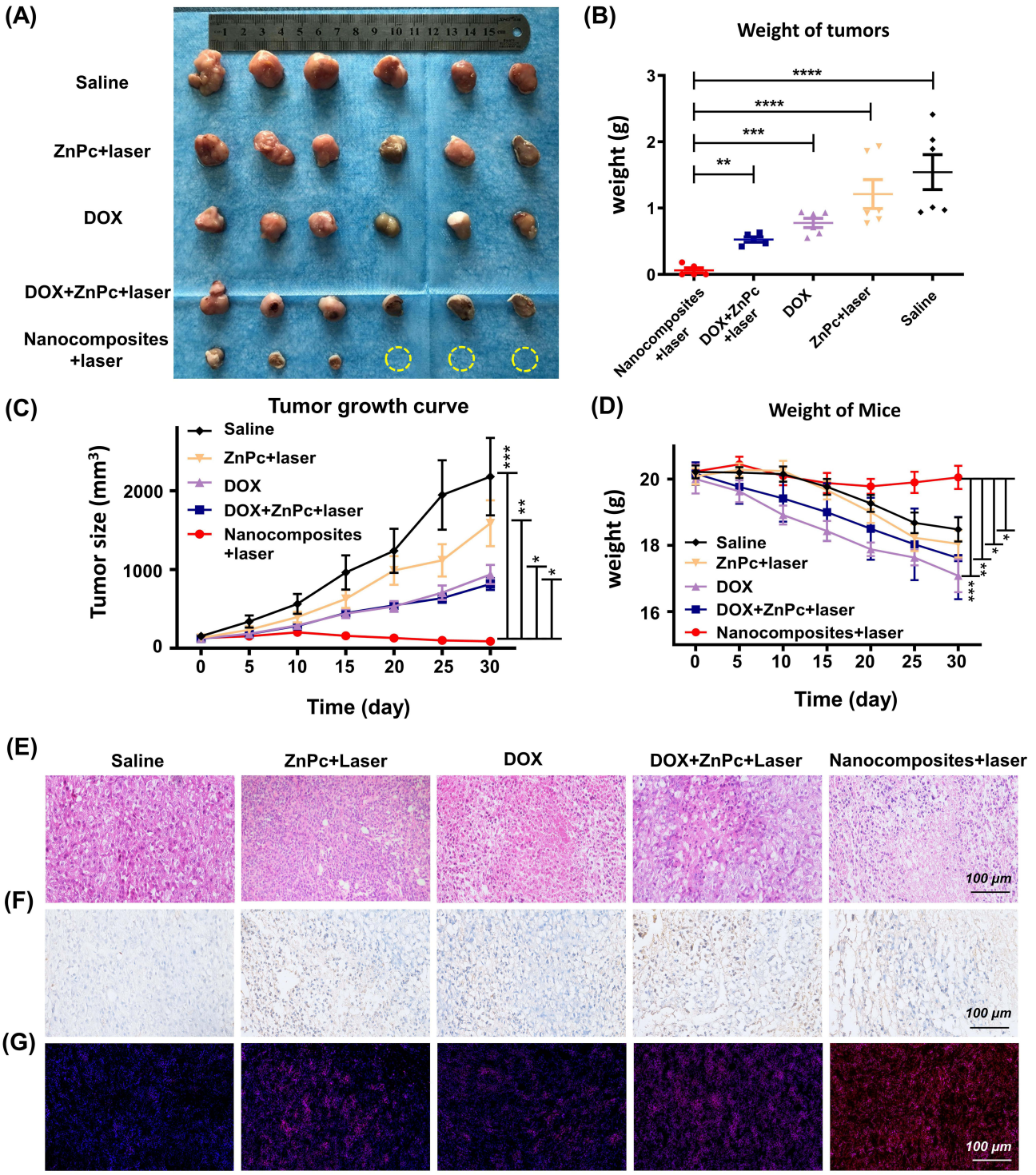

Figure 7 In vivo tumor suppression of DOX-HA/ZnPc-bMSN nanocomposites. (**A**) All of the remaining tumors after the intervention. Yellow dotted circles indicate completely cured tumors. (**B**) The tumor weighing results after the intervention (n = 6). (**C**) The tumor growth curves after the intervention (n = 6). (**D**) The mean weight changing curve of the mice during the experiment (n = 6). (**E**) H&E images of tumor tissues after treatments. (**F**) TUNEL images of tumor tissues after treatments. (**G**) ROS images of tumor tissues after treatments. Error bars represent the standard deviation of the mean. *$p < 0.05$, **$p < 0.01$, ***$p < 0.001$, ****$p < 0.0001$.

To further evaluate the therapeutic effects, tumor tissues from the different treatment groups were subjected to H&E staining, TUNEL staining, and ROS level detection. The results revealed that tumor tissues from mice treated with DOX-HA/ZnPc-bMSN nanocomposites+laser exhibited significantly greater inflammatory cell infiltration compared to the other groups (Figure 7E). Additionally, the number of TUNEL-positive cells was markedly higher (Figure 7F), and ROS

levels were significantly elevated (Figure 7G), consistent with the observations at the cellular level. Quantitative analysis using Image J software was performed on the number of TUNEL-positive cells (Supplementary Figure 7) and the fluorescence intensity of tissue ROS staining (Supplementary Figure 8). The apoptosis index in the DOX-HA/ZnPc-bMSN nanocomposites+laser group (59.9%) was 2.1 times higher than that in the DOX group (29.2%), 3.9 times higher than that in the ZnPc+laser group (15.3%), and 1.9 times higher than that in the DOX+ZnPc+laser group (32.1%). Furthermore, it was 4-fold higher than the apoptotic index (15%) achieved by the self-assembled porphyrin nanofibers developed by Liu et al.[59] The ROS production rate in the DOX-HA/ZnPc-bMSN nanocomposites+laser group was 5.3 times higher than that in the DOX group, 3.5 times higher than that in the ZnPc+laser group, and 1.9 times higher than that in the DOX+ZnPc+laser group. These findings align closely with the results obtained at the cellular level, further validating that the PDT and chemotherapy mediated by DOX-HA/ZnPc-bMSN nanocomposites effectively induce PC-3 cell apoptosis and suppress tumor cell proliferation by promoting ROS generation. Interestingly, the ROS production and apoptosis rates in the DOX group were lower than those in the ZnPc+laser group at the cellular level. However, in CCK-8 assays, colony formation assays, live/dead cell staining, and in vivo antitumor experiments, the tumor cell killing rate in the DOX group was slightly higher than that in the ZnPc+laser group. This observation may be explained by the additional mechanism by which DOX kills PC-3 cells through the inhibition of DNA replication.

To sum up, the synergistic strategy of PDT and CT has emerged as a crucial research direction for enhancing anti-tumor efficacy while reducing systemic toxicity. Recent studies on DOX/PS co-delivery systems have further validated the potential of this combined treatment modality.[60,61] Among numerous nanoplatforms, bMSN NPs stand out due to their tunable pore size, high specific surface area, easily modifiable surface, and excellent biocompatibility, making them ideal materials for constructing various nanocomposites.[62,63] Currently, multiple drug formulations based on bMSN NPs have entered clinical trial stages and demonstrated promising clinical efficacy and safety.[64,65] This highlights the significant safety, effectiveness, and clinical development prospects of bMSN NPs in biomedical applications. Additionally, HA, a natural linear polysaccharide primarily present in the extracellular matrix of various human tissues, can specifically bind to various tumor cells overexpressing CD44 and is degraded by HAase in vivo.[66] Compared with other CD44-targeting materials, HA offers advantages such as good biocompatibility, biodegradability, and low immunogenicity.[67] Given these merits, HA-based nanoparticles (HA NPs) have been widely used as carriers for tumor-targeted therapy.

In this study, the above materials were used to design a blackberry-like nanocomposite with a double-layer structure, successfully addressing the critical challenge of co-loading DOX and ZnPc with high efficiency. The nanocomposites achieve precise tumor targeting and sequential drug release, enabling sustained synergistic PDT-CT effects while simultaneously inducing both apoptosis and pyroptosis in tumor cells. These remarkable therapeutic outcomes, coupled with minimal toxicity, demonstrate significant clinical potential. However, several limitations must be acknowledged regarding clinical translation. Firstly, primary findings indicate that while CD44 shows significant overexpression in most tumor types compared to normal tissues, current research reports marked downregulation in specific tumor subtypes.[68] Consequently, the targeting efficiency of DOX-HA/ZnPc-bMSN nanocomposites may be impaired in CD44-low tumor subtypes. Furthermore, although HA-mediated CD44 targeting demonstrates promising therapeutic potential, its targeting efficacy remains suboptimal. These limitations could potentially be addressed by developing dual-targeting systems or incorporating high-affinity monoclonal antibodies to further enhance targeting specificity. Secondly, comprehensive long-term biodistribution studies are required to fully evaluate the biodegradation profile and potential chronic toxicity of DOX-HA/ZnPc-bMSN nanocomposites. Thirdly, while the adopted low-power-density (0.05 W/cm^2) and prolonged irradiation (2 hours) protocol effectively minimizes normal tissue damage, its clinical practicality may be constrained by patient compliance and treatment duration considerations. Most notably, scalable manufacturing presents a formidable challenge. The reproducible fabrication of the blackberry-like architecture demands precise control over electrostatic self-assembly and layer-by-layer coating processes - parameters that may prove difficult to maintain during large-scale production.

Conclusion

We successfully developed tumor-targeting blackberry-like nanocomposites (DOX-HA/ZnPc-bMSN) through electrostatic adsorption of doxorubicin-loaded hyaluronic acid nanoparticles (DOX-HA NPs) onto biodegradable mesoporous silica nanoparticles (bMSN NPs) pre-encapsulated with ZnPc. The nanocomposites exhibited a high ZnPc drug loading capacity (DLC: 10.2% ± 1.6%) and efficient tumor accumulation. They enabled long-term PDT and CT synergistic therapy with a remarkably low combination index (CI = 0.26). In vivo studies demonstrated 96.0% tumor inhibition under an ultralow-dose regimen (DOX: 0.2 mg/kg; ZnPc: 2 mg/kg) that proves the advantage of 2-hour extended PDT and related CT strategy. Notably, the LD50 of DOX-HA/ZnPc-bMSN nanocomposites (138.95 mg/kg) was 15.12-fold higher than that of free DOX, indicating significantly reduced systemic toxicity. Therefore, long-term PDT and CT synergistic therapy with nanocomposites demonstrates significant potential for future clinical applications. Future research should focus on optimizing the preparation processes for nanocomposites, refining preclinical experiments—such as extending biodistribution studies (beyond 96 hours) and chronic toxicity assessments—and exploring synergistic combinations with immunotherapy to facilitate clinical translation and ultimately benefit cancer patients.

Data Sharing Statement

The authors confirm that the data supporting the findings of this study are available within the article.

Acknowledgments

This work was supported, in part, by the Key Research and Development Program in Ningxia Province of China (No.2023BEG03035), the Natural Science Basic Research Key Program of Ningxia Province of China (No.2024AAC02079), the State Key Laboratory of Pathogenesis, Prevention and Treatment of High Incidence Diseases in Central Asia Fund (SKL-HIDCA-2024-NX1), the Beijing Dadi Medical Charity Foundation (DDYL-A-KT-20250107-0003), and the the Health Re-search Program on Ningxia (2025-NWQP-B002).

Author Contributions

All authors made a significant contribution to the work reported, whether that is in the conception, study design, execution, acquisition of data, analysis and interpretation, or in all these areas; took part in drafting, revising or critically reviewing the article; gave final approval of the version to be published; have agreed on the journal to which the article has been submitted; and agree to be accountable for all aspects of the work.

Disclosure

The authors report no conflicts of interest in this work.

References

1. Bray F, Laversanne M, Sung H, et al. Global cancer statistics 2022: GLOBOCAN estimates of incidence and mortality worldwide for 36 cancers in 185 countries. *CA Cancer J Clin*. 2024;74(3):229–263. doi:10.3322/caac.21834
2. DeVita VT, Chu E. A history of cancer chemotherapy. *Cancer Res*. 2008;68(21):8643–8653. doi:10.1158/0008-5472.CAN-07-6611
3. Chabner BA, Roberts TG. Timeline: chemotherapy and the war on cancer. *Nat Rev Cancer*. 2005;5(1):65–72. doi:10.1038/nrc1529
4. Holohan C, Van Schaeybroeck S, Longley DB, Johnston PG. Cancer drug resistance: an evolving paradigm. *Nat Rev Cancer*. 2013;13(10):714–726. doi:10.1038/nrc3599
5. Wu L, Wang L, Du Y, Zhang Y, Ren J. Mitochondrial quality control mechanisms as therapeutic targets in doxorubicin-induced cardiotoxicity. *Trends Pharmacol Sci*. 2023;44(1):34–49. doi:10.1016/j.tips.2022.10.003
6. Minotti G, Recalcati S, Menna P, Salvatorelli E, Corna G, Cairo G. Doxorubicin cardiotoxicity and the control of iron metabolism: quinone-dependent and independent mechanisms. *Methods Enzymol*. 2004;378:340–361. doi:10.1016/S0076-6879(04)78025-8
7. Indulekha S, Arunkumar P, Bahadur D, Srivastava R. Dual responsive magnetic composite nanogels for thermo-chemotherapy. *Colloids Surf B Biointerfaces*. 2017;155:304–313. doi:10.1016/j.colsurfb.2017.04.035
8. Pan M, Liu Y, Sang T, et al. Enhanced antitumor and anti-metastasis by VEGFR2-targeted doxorubicin immunoliposome synergy with NK cell activation. *Invest New Drugs*. 2023;41(5):664–676. doi:10.1007/s10637-023-01372-5
9. Bao YH, Guo ZF, Li JT, Zhang MZ, He JL, Ni PH. Combination antitumor therapy based on codelivery nanosystems of doxorubicin. *Prog Chem*. 2023;35(8):1123–1135. doi:10.7536/PC230114
10. Wilson BC, Patterson MS. The physics, biophysics and technology of photodynamic therapy. *Phys Med Biol*. 2008;53(9):R61–R109. doi:10.1088/0031-9155/53/9/R01

11. Li X, Lovell JF, Yoon J, Chen X. Clinical development and potential of photothermal and photodynamic therapies for cancer. *Nat Rev Clin Oncol*. 2020;17(11):657–674. doi:10.1038/s41571-020-0410-2
12. Niculescu AG, Grumezescu AM. Photodynamic therapy—an up-to-date review. *Appl Sci*. 2021;11(8):3626. doi:10.3390/app11083626
13. Skovsen E, Snyder JW, Lambert JD, Ogilby PR. Lifetime and diffusion of singlet oxygen in a cell. *J Phys Chem B*. 2005;109(18):8570–8573. doi:10.1021/jp051163i
14. Brodin NP, Guha C, Tomé WA. Photodynamic Therapy and Its Role in Combined Modality Anticancer Treatment. *Technol Cancer Res Treat*. 2015;14(4):355–368. doi:10.1177/1533034614556192
15. Carobeli LR, Santos ABC, Martins LBM, Damke E, Consolaro MEL. Recent advances in photodynamic therapy combined with chemotherapy for cervical cancer: a systematic review. *Expert Rev Anticancer Ther*. 2024;24(5):263–282. doi:10.1080/14737140.2024.2337259
16. Sekkat N, Van den Bergh H, Nyokong T, Lange N. Like a Bolt from the Blue: phthalocyanines in Biomedical Optics. *Molecules*. 2012;17(1):98–144. doi:10.3390/molecules17010098
17. Yang Z, Li P, Chen Y, et al. Preparation of zinc phthalocyanine-loaded amphiphilic phosphonium chitosan nanomicelles for enhancement of photodynamic therapy efficacy. *Colloids Surf B Biointerfaces*. 2021;202:111693. doi:10.1016/j.colsurfb.2021.111693
18. Huang Z, Xiao H, Lu X, Yan W, Ji Z. Enhanced photo/chemo combination efficiency against bladder tumor by encapsulation of DOX and ZnPC into in situ-formed thermosensitive polymer hydrogel. *Int J Nanomed*. 2018;13:7623–7631. doi:10.2147/IJN.S179226
19. Wang XY, Liu YR, Liu TY, Mustafa F, Guan QX. Doxorubicin and Zinc phthalocyanine loaded pH-responsive FA-BSP-SA/TPGS micelles for synergistic chemo-photodynamic therapy against tumors. *J Drug Deliv Sci Technol*. 2022;76:103713. doi:10.1016/j.jddst.2022.103713
20. Ma J, Chen D, Li Y, et al. Zinc phthalocyanine-soybean phospholipid complex based drug carrier for switchable photoacoustic/fluorescence image, multiphase photothermal/photodynamic treatment and synergetic therapy. *J Control Release*. 2018;284:1–14. doi:10.1016/j.jconrel.2018.06.005
21. Mroz P, Yaroslavsky A, Kharkwal GB, Hamblin MR. Cell death pathways in photodynamic therapy of cancer. *Cancers*. 2011;3(2):2516–2539. doi:10.3390/cancers3022516
22. Qi S, Guo L, Yan S, Lee RJ, Yu S, Chen S. Hypocrellin A-based photodynamic action induces apoptosis in A549 cells through ROS-mediated mitochondrial signaling pathway. *Acta Pharm Sin B*. 2019;9(2):279–293. doi:10.1016/j.apsb.2018.12.004
23. Igney FH, Krammer PH. Death and anti-death: tumour resistance to apoptosis. *Nat Rev Cancer*. 2002;2(4):277–288. doi:10.1038/nrc776
24. Ward RA, Fawell S, Floc'h N, Flemington V, McKerrecher D, Smith PD. Challenges and opportunities in cancer drug resistance. *Chem Rev*. 2021;121(6):3297–3351. doi:10.1021/acs.chemrev.0c00383
25. Fang Y, Tian S, Pan Y, et al. Pyroptosis: a new frontier in cancer. *Biomed Pharmacother*. 2020;121:109595. doi:10.1016/j.biopha.2019.109595
26. Wang Q, Wang Y, Ding J, et al. A bioorthogonal system reveals antitumour immune function of pyroptosis. *Nature*. 2020;579(7799):421–426. doi:10.1038/s41586-020-2079-1
27. Wang JS, Wu ZY, Zhu M, Zhao Y, Xie JW. ROS induced pyroptosis in inflammatory disease and cancer. *Front Immunol*. 2024;15:1378990. doi:10.3389/fimmu.2024.1378990
28. Li R, Zhang X, Zhu P, Ng DK, Kobayashi N, Jiang J. Electron-donating or -withdrawing nature of substituents revealed by the electrochemistry of metal-free phthalocyanines. *Inorg Chem*. 2006;45(5):2327–2334. doi:10.1021/ic051931k
29. Çamur M, Bulut M, Kandaz M, Güney O. Synthesis, characterization and fluorescence behavior of new fluorescent probe phthalocyanines bearing coumarin substituents. *Polyhedron*. 2009;28(2):233–238. doi:10.1016/j.poly.2008.10.066
30. Yue C, Liu P, Zheng M, et al. IR-780 dye loaded tumor targeting theranostic nanoparticles for NIR imaging and photothermal therapy. *Biomaterials*. 2013;34(28):6853–6861. doi:10.1016/j.biomaterials.2013.05.071
31. Chou TC. Drug combination studies and their synergy quantification using the Chou-Talalay method. *Cancer Res*. 2010;70(2):440–446. doi:10.1158/0008-5472.CAN-09-1947
32. Josefsen LB, Boyle RW. Photodynamic therapy and the development of metal-based photosensitisers. *Met Based Drugs*. 2008;2008:276109. doi:10.1155/2008/276109
33. Xu C, Chen F, Valdovinos HF, et al. Bacteria-like mesoporous silica-coated gold nanorods for positron emission tomography and photoacoustic imaging-guided chemo-photothermal combined therapy. *Biomaterials*. 2018;165:56–65. doi:10.1016/j.biomaterials.2018.02.043
34. Xu B, Li S, Shi R, Liu H. Multifunctional mesoporous silica nanoparticles for biomedical applications. *Signal Transduct Target Ther*. 2023;8(1):435. doi:10.1038/s41392-023-01654-7
35. Almeida PV, Shahbazi MA, Mäkilä E, et al. Amine-modified hyaluronic acid-functionalized porous silicon nanoparticles for targeting breast cancer tumors. *Nanoscale*. 2014;6(17):10377–10387. doi:10.1039/c4nr02187h
36. Pilco-Ferreto N, Calaf GM. Influence of doxorubicin on apoptosis and oxidative stress in breast cancer cell lines. *Int J Oncol*. 2016;49(2):753–762. doi:10.3892/ijo.2016.3558
37. Zhang Z, Zhang H, Li D, Zhou X, Qin Q, Zhang Q. Caspase-3-mediated GSDME induced Pyroptosis in breast cancer cells through the ROS/JNK signalling pathway. *J Cell Mol Med*. 2021;25(17):8159–8168. doi:10.1111/jcmm.16574
38. Shi Y, Van der Meel R, Chen X, Lammers T. The EPR effect and beyond: strategies to improve tumor targeting and cancer nanomedicine treatment efficacy. *Theranostics*. 2020;10(17):7921–7924. doi:10.7150/thno.49577
39. Tian Z, Yao X, Ma K, et al. Metal-organic framework/graphene quantum dot nanoparticles used for synergistic chemo-and photothermal therapy. *ACS Omega*. 2017;2(3):1249–1258. doi:10.1021/acsomega.6b00385
40. Li K, Liu H, Gao W, et al. Mulberry-like dual-drug complicated nanocarriers assembled with apogossypolone amphiphilic starch micelles and doxorubicin hyaluronic acid nanoparticles for tumor combination and targeted therapy. *Biomaterials*. 2015;39:131–144. doi:10.1016/j.biomaterials.2014.10.073
41. Ma J, Li Y, Liu G, et al. Novel theranostic zinc phthalocyanine-phospholipid complex self-assembled nanoparticles for imaging-guided targeted photodynamic treatment with controllable ROS production and shape-assisted enhanced cellular uptake. *Colloids Surf B Biointerfaces*. 2018;162:76–89. doi:10.1016/j.colsurfb.2017.10.061
42. Moodley T, Singh M. Sterically stabilised polymeric mesoporous silica nanoparticles improve doxorubicin efficiency: tailored cancer therapy. *Molecules*. 2020;25(3):742. doi:10.3390/molecules25030742
43. Ma J, Wu H, Li Y, et al. Novel core-interlayer-shell DOX/ZnPc Co-loaded MSNs@ pH-Sensitive CaP@PEGylated liposome for enhanced synergetic chemo-photodynamic therapy. *Pharm Res*. 2018;35(3):57. doi:10.1007/s11095-017-2295-z

44. An X, Zhu A, Luo H, Ke H, Chen H, Zhao Y. Rational design of multi-stimuli-responsive nanoparticles for precise cancer therapy. *ACS Nano*. 2016;10(6):5947–5958. doi:10.1021/acsnano.6b01296
45. Wang X, Tong J, He Z, et al. Paclitaxel-potentiated photodynamic theranostics for synergistic tumor ablation and precise anticancer efficacy monitoring. *ACS Appl Mater Interfaces*. 2020;12(5):5476–5487. doi:10.1021/acsami.9b19073
46. Gao D, Lo PC. Polymeric micelles encapsulating pH-responsive doxorubicin prodrug and glutathione-activated zinc(II) phthalocyanine for combined chemotherapy and photodynamic therapy. *J Control Release*. 2018;282:46–61. doi:10.1016/j.jconrel.2018.04.030
47. Cagel M, Grotz E, Bernabeu E, Moretton MA, Chiappetta DA. Doxorubicin: nanotechnological overviews from bench to bedside. *Drug Discov Today*. 2017;22(2):270–281. doi:10.1016/j.drudis.2016.11.005
48. Tan H, Hou N, Liu Y, et al. CD133 antibody targeted delivery of gold nanostars loading IR820 and docetaxel for multimodal imaging and near-infrared photodynamic/photothermal/chemotherapy against castration resistant prostate cancer. *Nanomedicine*. 2020;27:102192. doi:10.1016/j.nano.2020.102192
49. Wu M, Liu X, Chen H, et al. Activation of pyroptosis by membrane-anchoring AIE photosensitizer design: new prospect for photodynamic cancer cell ablation. *Angew Chem Int Ed Engl*. 2021;60(16):9093–9098. doi:10.1002/anie.202016399
50. Brennan MA, Cookson BT. Salmonella induces macrophage death by caspase-1-dependent necrosis. *Mol Microbiol*. 2000;38(1):31–40. doi:10.1046/j.1365-2958.2000.02103.x
51. Korbelik M, Banáth J, Zhang W, et al. N-dihydrogalactochitosan as immune and direct antitumor agent amplifying the effects of photodynamic therapy and photodynamic therapy-generated vaccines. *Int Immunopharmacol*. 2019;75:105764. doi:10.1016/j.intimp.2019.105764
52. Guo W, Li Z, Huang H, et al. VB12-Sericin-PBLG-IR780 nanomicelles for programming cell pyroptosis via Photothermal (PTT)/Photodynamic (PDT) effect-induced Mitochondrial DNA (mitoDNA) oxidative damage. *ACS Appl Mater Interfaces*. 2022;14(15):17008–17021. doi:10.1021/acsami.1c22804
53. Tan YX, Chen QZ, Li XL, et al. Pyroptosis: a new paradigm of cell death for fighting against cancer. *J Exp Clin Cancer Res*. 2021;40(1):153. doi:10.1186/s13046-021-01959-x
54. Ma CJ, Wang Y, Chen W, et al. Caspase-1 regulates the apoptosis and pyroptosis induced by phthalocyanine zinc-mediated photodynamic therapy in breast cancer MCF-7 cells. *Molecules*. 2023;28(16):5934. doi:10.3390/molecules28165934
55. Huang Y, Xie P, Yang ST, et al. Carbon nanoparticles suspension injection for the delivery of doxorubicin: comparable efficacy and reduced toxicity. *Mater Sci Eng C Mater Biol Appl*. 2018;92:416–423. doi:10.1016/j.msec.2018.07.012
56. Wang Y, Wu YS, Li K, Shen SH, Liu ZY, Wu DC. Ultralong circulating lollipop-like nanoparticles assembled with gossypol, doxorubicin, and polydopamine via π-π stacking for synergistic tumor therapy. *Adv Funct Mater*. 2019;29(1):1805582. doi:10.1002/adfm.201805582
57. Xiong LH, Yang L, Geng J, Tang BZ, He X. All-in-one alkaline phosphatase-response aggregation-induced emission probe for cancer discriminative imaging and combinational chemodynamic-photodynamic therapy. *ACS Nano*. 2024;18(27):17837–17851. doi:10.1021/acsnano.4c03879
58. Lu Z, Chen X, Wang C, et al. Self-assembled nanocomposite DOX/$TPOR_4$@$CB[7]_4$ for enhanced synergistic photodynamic therapy and chemotherapy in neuroblastoma. *Pharmaceutics*. 2024;16(6):822. doi:10.3390/pharmaceutics16060822
59. Liu X, Zhan W, Gao G, et al. Apoptosis-amplified assembly of porphyrin nanofiber enhances photodynamic therapy of oral tumor. *J Am Chem Soc*. 2023;145(14):7918–7930. doi:10.1021/jacs.2c13189
60. Cesca BA, Pellicer San Martin K, Caverzan MD, Oliveda PM, Ibarra LE. State-of-the-art photodynamic therapy for malignant gliomas: innovations in photosensitizers and combined therapeutic approaches. *Explor Target Antitumor Ther*. 2025;6:1002303. doi:10.37349/etat.2025.1002303
61. Cesca BA, Caverzan MD, Lamberti MJ, Ibarra LE. Enhancing therapeutic approaches in glioblastoma with pro-oxidant treatments and synergistic combinations: in vitro experience of doxorubicin and photodynamic therapy. *Int J Mol Sci*. 2024;25(14):7525. doi:10.3390/ijms25147525
62. Mamaeva V, Sahlgren C, Lindén M. Mesoporous silica nanoparticles in medicine–recent advances. *Adv Drug Deliv Rev*. 2013;65(5):689–702. doi:10.1016/j.addr.2012.07.018
63. Castillo RR, Vallet-Regí M. Functional mesoporous silica nanocomposites: biomedical applications and biosafety. *Int J Mol Sci*. 2019;20(4):929. doi:10.3390/ijms20040929
64. Bukara K, Schueller L, Rosier J, et al. Ordered mesoporous silica to enhance the bioavailability of poorly water-soluble drugs: proof of concept in man. *Eur J Pharm Biopharm*. 2016;108:220–225. doi:10.1016/j.ejpb.2016.08.020
65. Rastinehad AR, Anastos H, Wajswol E, et al. Gold nanoshell-localized photothermal ablation of prostate tumors in a clinical pilot device study. *Proc Natl Acad Sci U S A*. 2019;116(37):18590–18596. doi:10.1073/pnas.1906929116
66. Zhang W, Qiao H, Cui J, Zhang D, Li Y. The redox homeostasis-reshapable hyaluronic acid-drug conjugate augments chemo-photodynamic therapy. *Int J Biol Macromol*. 2025;310(Pt 4):143465. doi:10.1016/j.ijbiomac.2025.143465
67. Caliendo A, Camorani S, Ibarra LE, et al. A novel CD44-targeting aptamer recognizes chemoresistant mesenchymal stem-like TNBC cells and inhibits tumor growth. *Bioact Mater*. 2025;50:443–460. doi:10.1016/j.bioactmat.2025.04.027
68. Zhu YJ, Li SY, Yang SS, Du Y, Zhang ZY, Liu JY. CD44 on cancer stem cell is a potential immunological and prognostic pan-cancer biomarker. *Cancer Cell Int*. 2025;25(1):134. doi:10.1186/s12935-025-03748-4